# Spontaneous Formation of an Internal Shear Band in Ice Flowing Over Topographically Variable Bedrock

**Journal Article**

**Author(s):**
Liu, Emma Weijia; Räss, Ludovic (iD); Herman, Frédéric; Podladchikov, Yury; Suckale, Jenny

**Key Points:**

- Ice flowing over rough basal topography may spontaneously develop an internal shear band that connects topographic highs
- Two competing mechanisms control the energy balance in the shear band: vertical advective cooling and internal shear heating
- We summarize how basal topography and the rheological power-law exponent influence the internal shear band formation in a regime diagram

**Correspondence to:**

E. W. Liu,
liuwj@stanford.edu

**Author Contributions:**

**Conceptualization:** Emma Weijia Liu, Ludovic Räss, Jenny Suckale
**Formal analysis:** Emma Weijia Liu
**Funding acquisition:** Jenny Suckale
**Methodology:** Emma Weijia Liu, Ludovic Räss, Jenny Suckale
**Software:** Emma Weijia Liu, Ludovic Räss
**Supervision:** Jenny Suckale
**Validation:** Emma Weijia Liu
**Visualization:** Emma Weijia Liu
**Writing – original draft:** Emma Weijia Liu
**Writing – review & editing:** Emma Weijia Liu, Frédéric Herman, Yury Podladchikov, Jenny Suckale

# Spontaneous Formation of an Internal Shear Band in Ice Flowing Over Topographically Variable Bedrock

**Emma Weijia Liu[1]** , **Ludovic Räss[2,3]** , **Frédéric Herman[4]** , **Yury Podladchikov[5]** , and **Jenny Suckale[1]**

[1]Geophysics Department, Stanford University, Stanford, CA, USA, [2]Laboratory of Hydraulics, Hydrology and Glaciology (VAW), ETH Zurich, Zurich, Switzerland, [3]Swiss Federal Institute for Forest, Snow and Landscape Research (WSL), Birmensdorf, Switzerland, [4]Institute of Earth Surface Dynamics, University of Lausanne, Lausanne, Switzerland, [5]Institute of Earth Sciences, University of Lausanne, Lausanne, Switzerland

**Abstract** Ice surface speed increases dramatically from upstream to downstream in many ice streams and glaciers. This speed-up is thought to be associated with a transition from internal distributed deformation to highly localized deformation or sliding at the ice-bedrock interface. The physical processes governing this transition remain unclear. Here, we argue that highly localized deformation does not necessarily initiate at the ice-bedrock interface, but could also take the form of an internal shear band inside the ice flow that connects topographic highs. The power-law exponent $n$ in the ice rheology amplifies the feedback between shear heating and shear localization, leading to the spontaneous formation of an internal shear band that can create flow separation within the ice. We model the thermomechanical ice flow over a sinusoidal basal topography by building on the high-resolution Stokes solver FastICE v1.0. We compile a regime diagram summarizing cases in which a sinusoidal topography with a given amplitude and wavelength leads to shear band formation for a given rheology. We compare our model results to borehole measurements from Greenland and find evidence to support the existence of an internal shear band. Our study highlights the importance of re-evaluating the degree to which internal deformation contributes to total deformation in the ice column and to the flow-to-sliding transition.

**Plain Language Summary** On its way toward the ocean, ice speeds up dramatically from less than 1 m/year upstream to more than a kilometer per year downstream. In this paper, we investigate the physical processes controlling this speed-up. Specifically, we focus on the role of the bedrock topography and rheology in facilitating the transition from this slow to rapid motion. We use a two-dimensional numerical model to simulate the flow field within a slab of ice flowing down a ramp over a simplified topography. We find that including the bedrock topography can lead to a zone of highly localized deformation within the ice above topographic highs. We also find that a non-linear rheology amplifies this localization. We compare our model results to borehole measurements from Greenland and find evidence that supports the existence of this highly localized deformation zone. This study indicates that the localized deformation induced by bedrock topography and amplified by non-linear rheology could be one physical mechanism that governs the speed-up of the ice flow.

## 1. Introduction

The world's two largest ice sheets, Antarctica and Greenland, discharge most of their ice mass through fast-moving ice streams and mountain glaciers (Joughin et al., 2010; Rignot et al., 2011). On its path toward the ocean, ice initially moves at relatively low speeds of approximately 1 m/year (Rignot et al., 2011) but then speeds up dramatically reaching surface speeds of more than a kilometer per year (Joughin et al., 2003; Mouginot et al., 2014; Rignot et al., 2002). This speed-up is thought to be associated with a transition from internal distributed deformation to highly localized deformation at the ice-bedrock interface (Clarke, 1987; Whillans et al., 1987). This transition from slow flow inland to rapid sliding near the outlets is known as the flow-to-sliding transition.

One potential explanation for the flow-to-sliding transition is the thawing of the bed: Ice moving over a temperate bed can slide whereas ice frozen onto the bed must deform internally. Creep instability could cause thawing (Robin, 1955) because deformation is most pronounced in cold ice near the bed, leading to shear weakening and intensified deformation until the temperature reaches the pressure melting point (Clarke et al., 1977; Yuen &

Schubert, 1979). However, it remains unclear how viable this explanation is, as first mentioned by Nye (1971) and later substantiated by Larson (1980) and Fowler (2001) who showed that the local conservation of flux implies a reduction in shearing, translating into less energy release and refreezing. Bueler (2009) identified the advection of cold ice to the warm bed as the main impediment for a sudden transition to sliding, an argument further developed by Mantelli et al. (2019).

The work by Bueler (2009) and Mantelli et al. (2019) suggests that the flow-to-sliding transition does not happen suddenly, but gradually over an extended distance in the flow direction. Yet, the physical processes governing this transition and the scale over which it occurs remain unresolved. Clues come from borehole measurements (Doyle et al., 2018; Harrington et al., 2015; Hills et al., 2017; Law et al., 2023; Lüthi et al., 2002; Maier et al., 2019; Ryser et al., 2014) suggest a complex, depth-dependent velocity field in the ice above a topographically variable bed. Many factors may contribute to this variability, including the presence of sediments and sediment freeze-on (Carsey et al., 2002; Goodwin, 1993; Gow et al., 1979; Herron & Langway, 1979), subglacial hydrology (Doyle et al., 2018), seasonal cycles (Ryser et al., 2014), paleolithic history (Lüthi et al., 2002), and variable basal topography (Law et al., 2023). Here, we focus specifically on the role of variable topography as a first step toward a more complete understanding.

The goal of this study is to elucidate the impact of topographically uneven bedrock on ice flow acceleration by quantifying shear localization inside the ice using numerical simulations. Several prior studies have investigated the role of topography on the thermomechanical deformation of sliding ice (e.g., Gudmundsson, 1997; Helanow et al., 2020, 2021). Our work complements these existing contributions by focusing on flowing ice prior to the onset of sliding. We hypothesize that the intense deformation of cold ice flowing over sufficiently pronounced basal topography can lead to the formation of an internal shear band connecting topographic highs that accounts for most of the internal deformation within the ice. Similar to flow separation in sliding ice (Gudmundsson, 1997), we expect that the conditions for shear band formation to depend on both the basal topography and the rheology imposed, particularly the degree of nonlinearity embedded in the rheology through the power-law exponent $n$.

We test our hypothesis through numerical simulations, building on recent advances in simulating the thermo-mechanical deformation of ice at high resolution implemented in FastICE v1.0 (Räss et al., 2020). We add to the original release of FastICE v1.0 by incorporating a free surface and variable basal topography, as both features are critical for the physical process that we aim to understand. We capture the free ice surface using a level-set representation (Osher & Sethian, 1988; Sethian & Smereka, 2003) and the basal topography through an Immersed-Boundary Method (IBM) (Peskin, 1972, 2002). The deformation of ice depends sensitively on ice rheology, because different rheological formulations can imply orders of magnitude differences in the response of ice deformation to stress. We consider ice rheology with power-law exponents from $n = 1$ to 4, representing the range of values identified in experiments and field data (Adams et al., 2021; Bons et al., 2018; Goldsby & Kohlstedt, 2001; Millstein et al., 2022; Pettit & Waddington, 2003).

Law et al. (2023) provide compelling evidence for complex, depth-dependent ice motion for three locations in Greenland, Sermeq Kujalleq/Store Glacier and Isunnguata Sermia Glacier, consistent with the idea of flow separation presented by Gudmundsson (1997). By linking field observations and numerical simulations, Law et al. (2023) show that both the vertical extent of temperate ice near the bed and the portion of deformation accommodated by basal slip vary significantly at the field-site scale and call for an improved parameterization of this variability in ice-sheet models. Law et al. (2023) also show that commonly used bedrock topography such as BedMachine (Morlighem et al., 2017) is too coarse and smooth. Using a geostatistically more accurate realization of bedrock topography results in rougher bedrock and enhanced shear localization.

Our study complements this compelling field evidence with an improved understanding of the physical processes that govern how the observed complexities in depth-dependent ice motion form. We intentionally focus on an idealized sinusoidal topography to advance this process-based understanding. Using both numerical simulations and scaling analysis, we propose a regime diagram that summarizes how the formation of an internal shear band depends on both the amplitude and wavelength of the underlying basal topography and the assumed ice rheology. Our analysis suggests that complex, depth-dependent deformation might not be unique to the specific field sites discussed in Law et al. (2023), but could be common when ice flows over a topographically pronounced bed. This finding highlights the importance of re-evaluating the degree to which internal deformation contributes to the total deformation in the ice column and to the transition from flow to sliding.
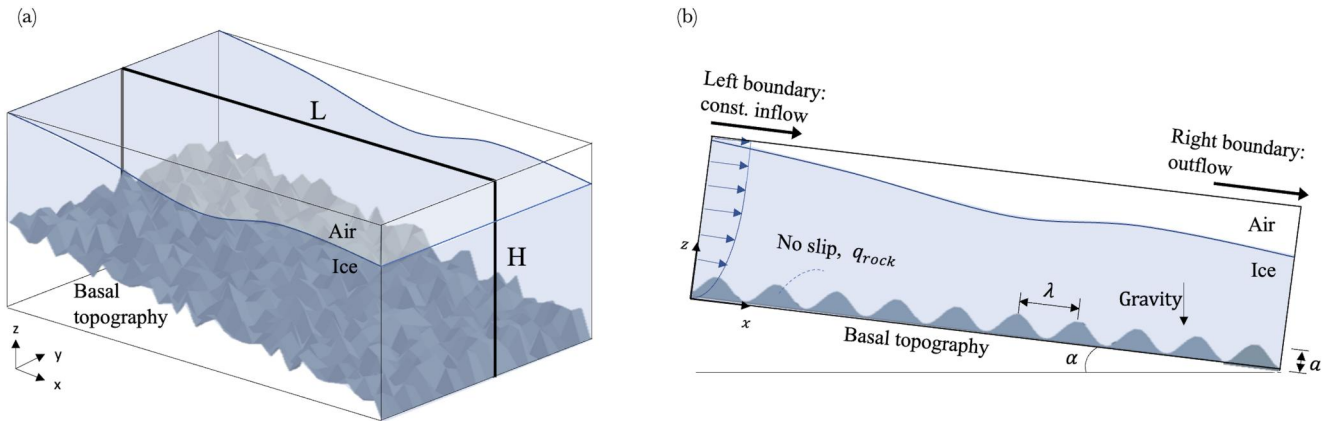
**Figure 1.** Model geometry of ice flowing over hard bedrock. (a) General case of an ice slab flowing over hard bedrock in three-dimensions with a free surface. (b) Two-dimensional model setup with a sinusoidal basal topography and a free surface.

## 2. Methods

To approximate the thermomechanical deformation within a slab of ice flowing over a rough hard bedrock in the downstream direction $x$, we neglect variability in the transverse direction $y$. This choice reduces our modeling domain to a two-dimensional along-flow cut through the three-dimensional ice slab along the thick black line as shown in Figure 1a. The depth direction $z$ is oriented vertically upward from the bedrock. The origin of the axes $(x = 0, z = 0)$ denotes the bedrock at the flow inlet. The size of the model domain is $[0, L] \times [0, H]$ tilted at an angle $\alpha$. To represent the basal topography, we adopt an idealized sinusoidal contour

$$z_b = a \sin(kx), \tag{1}$$

where $a$ is the amplitude and $k$ is the wavenumber. We include a thin layer of a low viscosity phase on top of the ice to mimic the presence of air, which allows the ice thickness to change spatially and temporally.

We solve for the thermomechanical ice deformation through an incompressible viscous Stokes solver based on implicit pseudo-transient methods and a finite difference discretization (Räss et al., 2020, 2022). To prescribe the ice-bedrock boundary condition, we implement the IBM, a fictitious domain method that allows us to treat fluid and solid domains separately (Peskin, 1972, 2002). To incorporate the free surface boundary condition, we use the level-set method, an implicit description for moving fronts (Osher et al., 2004; Sethian & Smereka, 2003). We discuss the implementations of the ice-bedrock and ice-air boundary conditions in Appendix A.

We describe ice as an incompressible, nonlinear, viscous fluid with a temperature-dependent rheology. The momentum equations are

$$\frac{\partial \tau_{ij}}{\partial x_j} - \frac{\partial p}{\partial x_i} + F_i = 0, \qquad \tau_{ij} = 2\eta \dot{\epsilon}_{ij}, \tag{2}$$

where $F_i = \rho g(\sin \alpha, \cos \alpha)$ is the gravitational body force at a tilted angle $\alpha$, $p$ is the isotropic pressure, $\tau_{ij}$ is the deviatoric stress tensor, $\dot{\epsilon}_{ij}$ is the strain rate tensor, $\eta$ is the ice viscosity, and $i \in \{x, z\}$ indexes the two spatial components. Reducing the model to two dimensions implies that all components in the transverse direction $y$ are zero. The only non-zero shear strain rate and shear stress are $\dot{\epsilon}_{zx}$ and $\tau_{zx}$, respectively.

Ice flows into the domain from the left boundary over undeforming bedrock and exits at the right boundary. We calculate the analytical inflow field by solving the momentum balance along the flow at steady state

$$\eta(z)\frac{\partial u}{\partial z} = \rho g(H - z)\sin \alpha, \quad \eta(z) = \eta_b + (\eta_s - \eta_b)\frac{z}{H}, \tag{3}$$

where we assume a linear viscosity profile between the viscosity at the bed, $\eta_b$, and the viscosity at the surface, $\eta_s$. By integrating Equation 3, we obtain the analytical inflow velocity in $x$ direction

$$u_{\text{inlet}} = \frac{\rho g \sin \alpha}{K^2} \big[ \eta_b \log(\eta_b + Kz) + KH \log(\eta_b + Kz) - Kz \big] + C, \tag{4}$$

where $K = (\eta_s - \eta_b)/H$ and $C$ is an integration constant that ensures a zero $x$ velocity at the bed. The inflow $z$ velocity is set to zero throughout the depth. When the viscosity is constant throughout the domain, $\eta_s = \eta_b = \eta_0$, the analytical inflow speed simplifies to a parabolic profile, $u_{\text{inlet}} = \rho \sin \alpha / \eta_0 (Hz - 0.5z^2)$.

At the outlet, we adapt the outflow boundary condition from Orlanski (1976):

$$\frac{\partial u}{\partial t} + U \frac{\partial u}{\partial x} = 0, \tag{5}$$

where $U$ is the propagation speed. We follow Kreiss (1968)'s implementation to estimate the propagation speed. The details of the implementation can be found in Appendix A.

At the ice surface, we assume that the atmospheric pressure is negligible relative to the pressure in the ice column, implying a stress-free surface

$$\sigma_{ij} n_j = 0, \tag{6}$$

where $n_j$ is a vector normal to the ice surface and $\sigma_{ij}$ is the Cauchy stress tensor, obtained by combining the isotropic pressure $p$ and the deviatoric stress $\tau_{ij}$. We do not account for accumulation or ablation because our model focuses on the kilometer scale where these would be approximately constant. Our main motivation for including a free surface is to resolve the cooling effect associated with dynamic thinning (Bueler, 2009; Mantelli et al., 2019). We impose a constant atmospheric temperature at the ice surface $T_s = -26°C$, a representative surface temperature in Antarctica.

At the ice-bedrock interface, we assume that the ice is frozen to bed and impose a no-slip boundary condition

$$u(z_b) = 0, \tag{7}$$

where $z_b$ is the bed elevation. In addition, we impose a constant geothermal heat flux

$$\kappa \frac{\partial T}{\partial x_j} n_j = q_{in}, \tag{8}$$

where $n_j$ the normal vector to the ice-bed interface.

The thermal model takes into account the effects of diffusion, advection, shear heating, and melt water weakening. We curtail the temperature at $T_m = -0.1°C$ and estimate the melt rate with the latent heat. The energy equation is given by

$$\rho c_p \left( \frac{\partial T}{\partial t} + u_i \frac{\partial T}{\partial x_i} \right) = \frac{\partial}{\partial x_i} \left( \kappa \frac{\partial T}{\partial x_i} \right) + 2\tau_E \dot{\epsilon}_E - L\dot{m}, \tag{9}$$

where $c_p$ is the specific heat of ice, $\kappa$ is the thermal conductivity, and $\tau_E$ and $\dot{\epsilon}_E$ are effective stress and effective strain rate, respectively. The term $2\tau_E \dot{\epsilon}_E$ represents shear heating, and $L\dot{m}$ captures the energy required for melting where $L = 0.366 \times 10^6$ J/kg is the latent heat and $\dot{m}$ is the generated melt water flux.

In the temperate zone, where the temperature is near the melting point, as defined by the logistic function

$$f(T - T_m) = 1 - \tanh(-0.5(T - T_m)), \tag{10}$$

we assume that the shear heating $2\tau_E\dot{\epsilon}_E$ is absorbed for the phase change from ice to water (Räss et al., 2020; Suckale et al., 2014). Hence, the temperature in the temperate zone cannot exceed the temperature at the pressure melting point, leading to a simplified energy equation

$$\rho c_p\left(\frac{\partial T}{\partial t} + u_i\frac{\partial T}{\partial x_i}\right) = \frac{\partial}{\partial x_i}\left(\kappa\frac{\partial T}{\partial x_i}\right) + 2\tau_E\dot{\epsilon}_E f(T - T_m). \tag{11}$$

The logistic Equation 10 serves as an indicator of how close the ice temperature is to the melting point $T_m$. When the temperature has reached the melting point, that is, $f(T - T_m) = 0$, all shear heating is absorbed for the phase change from ice to water, and no net heat source is added to the energy equation.

The time dependence of this problem arises from the free surface evolution and from the energy equation because the shear heating, diffusion, and advection terms are transient. At each physical time step, we apply the pseudo-transient method (Räss et al., 2022) to iteratively solve the system of the coupled momentum Equation 2 and energy Equation 11 until the continuity residual $\partial p/\partial\mathcal{T}_p$, momentum residual $\partial u_i/\partial\mathcal{T}_u$, and temperature residual $\partial T/\partial\mathcal{T}_T$ are minimized, achieving an implicit solution of the equations. Thus, the governing equations in residual form are

$$\frac{\partial p}{\partial\mathcal{T}_p} = -\frac{\partial u_i}{\partial x_i}, \tag{12}$$

$$\frac{\partial u_i}{\partial\mathcal{T}_u} = \frac{\partial\tau_{ij}}{\partial x_j} - \frac{\partial p}{\partial x_i} + F_i, \tag{13}$$

$$\frac{\partial T}{\partial\mathcal{T}_T} = -\frac{\partial T}{\partial t} - u_i\frac{\partial T}{\partial x_i} + \frac{1}{\rho c_p}\left(\frac{\partial}{\partial x_i}\left(\kappa\frac{\partial T}{\partial x_i}\right) + 2\tau_E\dot{\epsilon}_E f(T - T_m)\right), \tag{14}$$

where $\mathcal{T}$ presents the pseudo-time step and $t$ represents the physical time step. A detailed discussion of pseudo-time steps and how to set them can be found in Räss et al. (2020).

The key limiting factor for the convergence rates of Equations 12–14 is the nonlinear ice viscosity. During iterations in pseudo-time, we do not evolve the ice surface. After the residuals fall below the defined thresholds indicating that the numerical solution has reached the steady state, we advect the free surface with the local ice velocity, as discussed in more detail in Appendix A.

We implement a power-law relationship for the ice rheology using

$$\dot{\epsilon}_{ij} = A\tau_{II}^{n-1}\tau_{ij}, \tag{15}$$

where $A$ is the prefactor, $n$ is the power-law exponent, and $\tau_{II} = \sqrt{0.5\tau_{ij}\tau_{ij}}$ is the second invariant of the stress tensor.

One challenge in implementing the power-law rheology is that the prefactor $A$ is difficult to constrain experimentally or observationally, partly because it captures several different physical processes, such as grain size, temperature, ice fabrics, and other variables (Paterson, 1994). In our model, $A$ depends only on temperature and interstitial water content, and we neglect other dependencies mostly because there are only limited data to constrain it. We capture the temperature dependency of $A$ through the Arrhenius relationship and define an additional parameter $A_w$ to include the viscosity-weakening effect of interstitial water

$$A = A_0 A_w \exp\left(-\frac{Q}{R(T_s + T)}\right), \tag{16}$$

where $Q$ is the activation energy, $R$ is the universal gas constant, and $T_s$ is the surface temperature. The water weakening term takes the form of $A_w = 1 - f(T - T_m)$, where $f$ is the same logistic function as defined in Equation 10. $A_0$ is treated as a constant and comes from other dependencies such as the dependencies on grain size and ice fabrics.

The value of $A_0$ must adapt to the change in exponent $n$ to ensure that the flow fields, such as velocity and stress, do not become artificially large or small. One approach is to ensure that the reference deformation remains the same, regardless of the choice of parameter values (Zeitz et al., 2020). In our simulations, we follow a similar idea by manually calibrating the prefactor $A_0$ to ensure that the surface speed at the outflow boundary is on the same order of magnitude of approximately 60–80 m/year for different values of $n$ and different basal topographies.

We note that interstitial water can impact not only the prefactor $A$, but also the exponent $n$. In fact, Adams et al. (2021) suggests that the exponent for temperate ice with sufficient interstitial water is close to 1.1. Other studies have also found similar enhancements in creep rates as ice approaches the pressure melting point (e.g., Barnes et al., 1971; Mellor & Testa, 1969). However, because there are only limited data to accurately constrain the effect of interstitial water on the value of $n$, our model does not consider this effect.

## 3. Results

We set the physical domain size to 4,800 m by 850 m across all simulations in this section. The ice and the air thicknesses are initialized to be 800 and 50 m in the tilted $x - z$ plane, respectively. The surface temperature is prescribed as $-26°C$ as a representative value for the surface temperature in Antarctica. Additionally, we apply a geothermal heat flux of 0.05 W/m$^2$ (Maule et al., 2005; Shapiro & Ritzwoller, 2004; Wright et al., 2012). We represent variable basal topography as $z_b = a \sin(kx)$, with an amplitude of $a = 100$ m and a wavenumber $k$ ranging from 0.52 to 6.28.

For all simulations, we assume no-slip boundary conditions at the bed and a free surface. One example of the ice surface evolving over time can be found in Figure C1. At the scale of the model domain, the change in ice surface is not immediately apparent, but a close-up view of the upper tens of meters of the domain shows that the surface evolves, if only by a few meters or less than 1% of the ice thickness.

### 3.1. Topographic Undulations Can Induce Internal Shear Band Formation

To identify how basal topography affects internal deformation, we compare the thermomechanical deformation of ice flowing over an idealized sinusoidal topography to ice flowing over a flat bed (Figure 2). All other parameters and boundary conditions are identical for the two cases. For this comparison, we use a power-law rheology with exponent $n = 3$ (Glen, 1952, 1955) and include water weakening in the effective viscosity as discussed in Section 2.

Figure 2a shows the case of ice (light blue) flowing over a sinusoidal topography (dark gray) for the lower portion of our model domain. The ice speeds up from left to right as indicated by the green $x$ velocity profiles at four different along-flow locations of $x = 518, 1,873, 3,247, 4,273$ m, where we compare the local $x$ velocity in thick green lines with the inflow $x$ velocity in thin green lines. This speed-up is facilitated by the localization of the shear strain rate $\partial u/\partial z$ on top of the topography as indicated in dark blue. Here, we normalize the shear strain rate by the characteristic shear strain rate $\bar{\dot{\epsilon}}_{xz}$ (see Appendix D for characteristic values selection). Shear localizes near topographic highs, effectively linking up into a continuous zone of elevated shear strain rate above the topography. The control simulation of ice flowing over a flat bed is shown in Figure 2b. Similarly, ice speeds up as it flows downstream, aided by shear localization immediately above the flat topography.

The main difference between the two simulations is how shear localization $\partial u/\partial z$ is distributed with depth (Figure 2c). For the flat bed (Figure 2b), the shear strain rate is highest nearest to the bed, whereas topography shifts the shear strain rate maximum into the ice column to a depth that roughly corresponds to the height of the topographic peaks (Figure 2a). Both modes of deformation are capable of generating approximately comparable surface speeds of around 70 m/year, with the ice flowing over rough topography moving slightly faster at equal driving stress. Because the speed-up of the ice is gradual and not instantaneous, the cooling effect associated with ice thinning is not sufficient to prevent viscosity weakening in either of the simulations.

To quantify the share of total shear deformation accommodated within the ice as it flows over the basal topography, we define $\tilde{R}_d$ as the percentage of internal deformation in the ice column. This parameter is calculated as the ratio of the integral of the shear strain rate from the bed up to some elevation $z$ and the integral of the total shear strain rate throughout the entire ice column
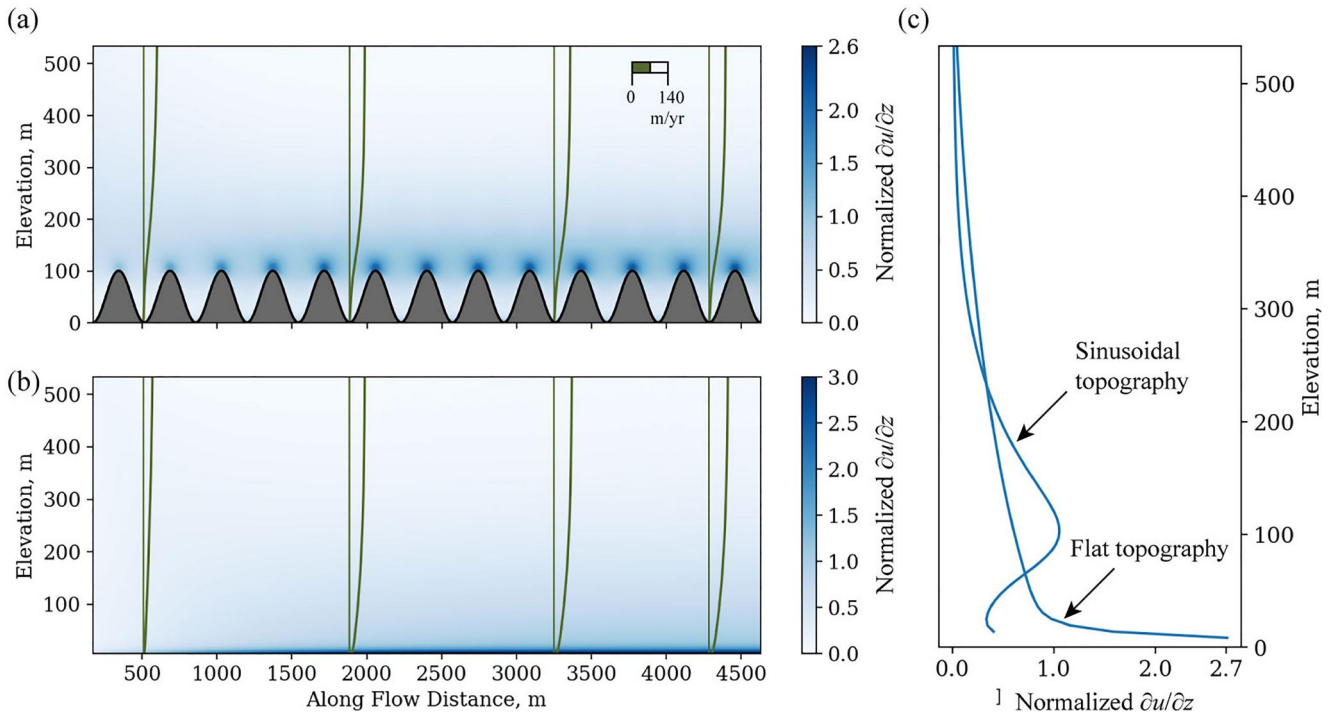
**Figure 2.** Role of basal topography in shear localization. (a, b) Normalized shear strain rate $\partial u/\partial z$ in the background contour for the case of with a sinusoidal basal topography and a flat basal topography. The $x$ velocity profiles at different locations along the flow are shown by thick green lines, with the reference inflow $x$ velocity by thin green lines. (c) Normalized shear strain rate profile at $x = 4,273$ m for both cases. We use the characteristic shear strain rate $\bar{\dot{\epsilon}}_{xz}$ (see Equation 19) for normalization.

$$\tilde{R}_d = \frac{\int_b^z \frac{\partial u}{\partial z}}{\int_b^s \frac{\partial u}{\partial z}} = \frac{u(z)}{u(H)}, \tag{17}$$

where the subscripts $d$, $b$, and $s$ represent deformation, bed, and surface, respectively. The tilde denotes it is a non-dimensional parameter. This parameter can also be interpreted as a velocity ratio with the local $x$ velocity divided by the $x$ velocity at the surface in the same ice column.

We use the term "shear band" to indicate a basal zone that accommodates the majority ($\geq 50\%$) of the total deformation in the ice column. We set the lower and upper bounds of the internal shear band $\tilde{R}_{dl}$ and $\tilde{R}_{du}$ to 20% and 70%, respectively. Finally, we define the band width $B_w$ as the vertical distance between these two bounds

$$B_w = z\left(\tilde{R}_{du}\right) - z\left(\tilde{R}_{dl}\right). \tag{18}$$

Figure 3 shows how the shear band evolves within the computational domain. Toward the left boundary, shear deformation is distributed relatively evenly, as indicated by the 20% and 70% contour lines, which differ by several hundred meters in depth (Figure 3a). As ice flows downstream, the lower limit of the shear band, $\tilde{R}_{dl} = 20\%$, stays on top of the basal topography shape and its location in the ice column shows little change. This result highlights that the depth-distribution of shear deformation below the topographic highs remains relatively unaffected by the shear localization and that the ice speeds up mainly at and above the topographic highs. The upper limit $\tilde{R}_{du} = 70\%$ descends sharply and then stabilizes at around $z = 200$ m. For the case shown, the shear band has a width that is close to the amplitude of the sinusoidal bed shape, and accommodates approximately half of the total shear deformation.

In the control case without topography, shear deformation also localizes due to viscosity weakening, but the shear band is located at the bed instead of within the ice column. The shear strain rate is maximal at the ice-bedrock
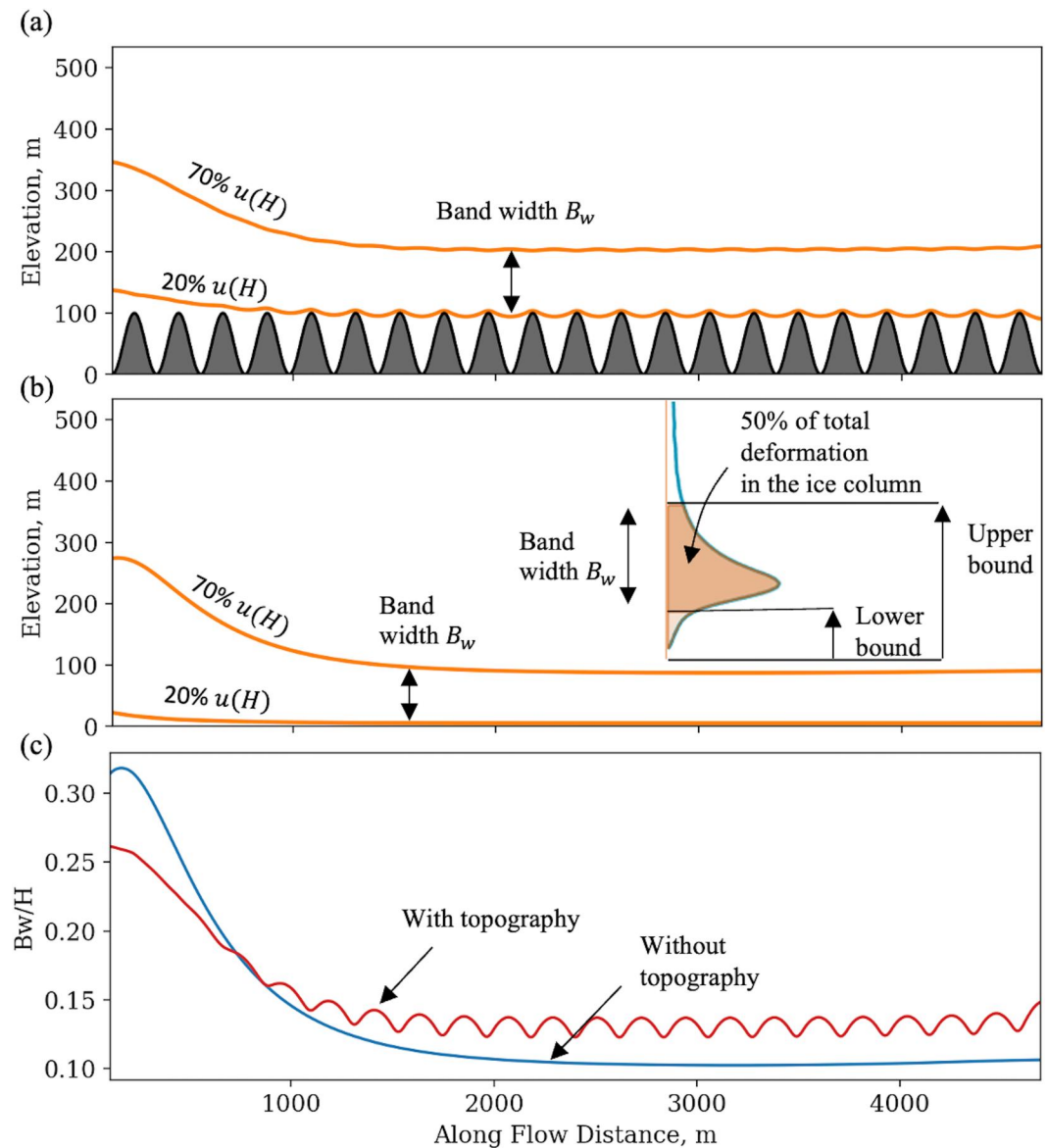
**Figure 3.** Shear band development along the flow. (a, b) Shear band development with and without a topography, defined as a basal zone in which 50% of the total deformation in the ice column occurs. We define the lower and upper boundary of the shear band to be 20% and 70% of the deformation in the ice column, as illustrated in the sub-panel in (b). (c) Ratio of the shear band width $B_w$ to the ice thickness $H$ at a given location along the flow for both cases.

interface with the $\tilde{R}_{dl} = 20\%$ contour remaining very close to and almost at the bed (Figure 3b). Figure 3c shows the ratio of the shear band width $B_w$ to the ice thickness $H$. Initially, the shear band width constitutes about 30% of the ice thickness for both cases. The width decreases rapidly in the downstream direction, and finally stabilizes at a width of approximately 10% of the ice thickness.

### 3.2. An Increasing Power-Law Exponent Amplifies Shear Localization

Similar to the creep instability, shear band formation is driven by the positive feedback that localized deformation reduces ice viscosity, which further localizes the deformation. This feedback depends on the degree to which ice in the vicinity of topographic highs warms up when flowing, as captured in the energy Equation 11. Three terms contribute to the thermal evolution: advection, diffusion, and shear heating. Through a simple scaling analysis (see Appendix D), we find that vertical advection and shear heating are the two primary competing terms in our
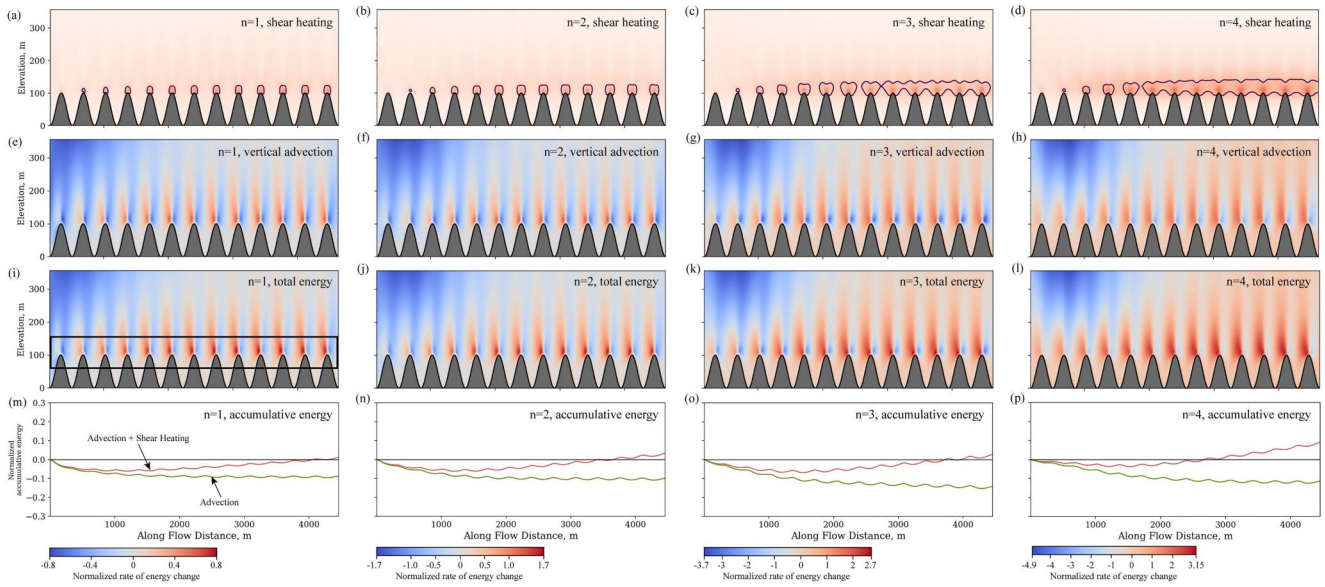
**Figure 4.** Role of the power-law exponent $n$ in normalized shear heating $\tilde{\mathcal{H}}_s$, vertical advection $\tilde{\mathcal{C}}_v$, and total energy $\tilde{\mathcal{E}}$ as defined in Equation 20. First row (a–d) Normalized shear heating $\tilde{\mathcal{H}}_s$ contours in the $x - z$ plane. The black contour lines denote half of the maximum of $\tilde{\mathcal{H}}_s$ in the computational domain. Second row (e–h) Normalized vertical advection $\tilde{\mathcal{A}}_v$ contours. Third row (i–l) Normalized total energy $\tilde{\mathcal{E}}$ contours. Fourth row (m–p) Depth averaged net energy gain (red curves) and accumulative vertical advection (green curves) along $x$ axis. The averaged area is indicated as the black box for $z = 80$–180 m in (i). Each column represents a different value of $n$ as indicated in each panel. All simulations have the same basal topography of $ak = 1.83$, where $ak$ is defined as the product of the amplitude and wavenumber of the bed.

case. In comparison, diffusion is roughly two orders of magnitude smaller than these two terms. Therefore, we approximate the total energy as the combined contributions of only vertical advection and shear heating.

To meaningfully compare the magnitude of vertical advection and shear heating for different values of power-law exponent $n$ from 1 to 4, we first divide the shear heating term $2\tau_E\dot{\epsilon}_E$ by $\rho c_p$ to ensure that both terms have the same units of K/s. We pick the characteristic shear stress to be $\rho g H \sin \alpha$. The characteristic surface velocity and characteristic strain rate are then

$$\bar{U}_s = \frac{2(\rho g \alpha)^n A_0 H^{n+1}}{n+1}, \quad \bar{\dot{\epsilon}}_{xz} = \frac{(\rho g \alpha)^n A_0 H^{n+1}}{B_w(n+1)}. \tag{19}$$

Please see Appendix D for a detailed description of the characteristic values. The non-dimensional shear heating, vertical advection, and total energy can then be expressed as

$$\tilde{\mathcal{H}}_s = \frac{2\tau_E\dot{\epsilon}_E}{\rho g H \bar{\dot{\epsilon}}_{xz} \sin \alpha}, \quad \tilde{\mathcal{C}}_v = \frac{\partial T}{\partial z} \frac{u_z c_p}{g H \bar{\dot{\epsilon}}_{xz} \sin \alpha}, \quad \tilde{\mathcal{E}} = \tilde{\mathcal{H}}_s + \tilde{\mathcal{C}}_v, \tag{20}$$

where $\mathcal{H}_s$ is shear heating, $\mathcal{C}_v$ is vertical advection, $\mathcal{E}$ is the total energy, $u_z$ is the $z$ velocity, and a tilde represents a non-dimensional quantity. Figure 4 compares the rate of normalized energy change attributed to only shear heating (first row), only vertical advection (second row), and the total energy (third row) for values of $n$ ranging from 1 to 4 (columns 1–4).

In Figures 4a–4d, the black contour lines highlight half of the maximum shear heating value in the computational domain. The shear heating is positive throughout the domain and concentrates within the internal shear band extending on top of the topographic highs. The magnitude of heating tends to increase in the downstream direction. Notably, for $n = 1$, shear heating at topographic highs is minimal. As the value of $n$ increases, these localized shear heating regions begin to connect and form a band situated above the topography. For example, in Figure 4, zones of elevated shear heating begin to bridge when $n \geq 3$.
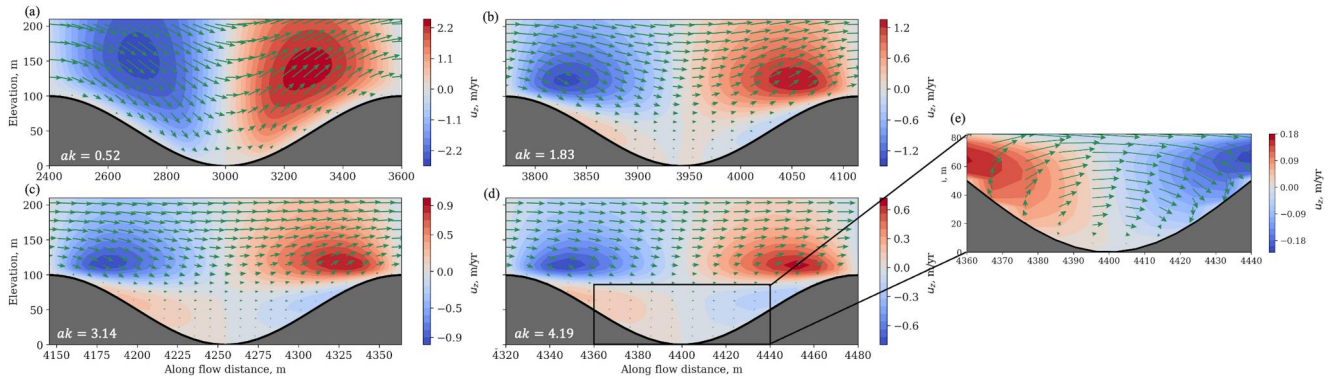
**Figure 5.** Role of basal topography shape in flow separation for $n = 3$. Each panel presents the vertical velocity contours and velocity vectors corresponding to a specific value of the shape factor $ak$, namely 0.52 (a), 1.83 (b), 3.14 (c), and 4.19 (d). (e) Shows a zoomed-in perspective of the bottom of the trough in (d).

The primary effect of vertical advection is cooling (Figures 4e–4h), particularly in the left third of the computational domain where cold ice is drawn down from the surface. This cooling effect is also reflected in the dipping of the iso-velocity-ratio lines in Figures F1 and F2. In the immediate vicinity of topographic highs, however, vertical advection is positive on the stoss side of the obstacle and negative on the lee side, as evidenced by the alternating blue and red regions.

Summing the shear heating and vertical advection produces the approximate total energy, which indicates the energy budget of the basal ice (Figures 4i–4l). The impact of shear heating is primarily confined to the vicinity of the basal topography, as deformation is predominantly concentrated near the bed. However, upon closer examination, it becomes evident that the lee side of the bumps, characterized by negative advection, is partially balanced by shear heating. The stoss side of the bumps, dominated by positive advection, experiences reinforcement.

We calculate the depth-averaged cumulative quantities for the shear heating and vertical advection within the specified range from $z_1$ to $z_2$, as indicated by the black box in Figure 4i

$$\overline{\mathcal{H}}_s(x) = \int_0^x \frac{1}{z_2 - z_1} \int_{z_1}^{z_2} \tilde{\mathcal{H}}_s \, dz \, dx, \quad \overline{\mathcal{C}}_v(x) = \int_0^x \frac{1}{z_2 - z_1} \int_{z_1}^{z_2} \tilde{\mathcal{C}}_v \, dz \, dx. \tag{21}$$

This cumulative measure serves as an indicator of the energy budget carried by the ice as it flows downstream. To focus on the basal region of interest, we select a depth-averaged range of 80–180 m, setting the interval to align with the amplitude of the sinusoidal bed.

Figures 4m–4p depict the energy budget profiles, where the green curves represent $\overline{\mathcal{C}}_v$, considering only vertical advection, and the red curves represent $\overline{\mathcal{E}}$, considering both vertical advection and shear heating. $\overline{\mathcal{C}}_v$ consistently exhibits negative values for all values of $n$, indicating that the ice within the basal region does not experience a positive energy gain. However, when incorporating shear heating alongside vertical advection, $\overline{\mathcal{E}}$ gradually becomes positive in the downstream direction. This trend holds true across all values of $n$, although higher values of $n$ tend to amplify the extent of total energy.

One important implication of shear band formation is a separation of the flow in the ice: The ice above the shear band moves relatively fast and is characterized by a simple flow field dominated by a speed-up in the flow direction. In contrast, basal ice slows down as the shear band accommodates the majority of the deformation. The flow field in the basal ice underneath the shear band is more complex. Figure 5 shows how the degree of flow separation varies for four different topographies defined by the shape factor $ak$ that represents the product of the amplitude and wavelength of the bed. We show the flow field only for a single trough with shape factors $ak$ of 0.52, 1.83, 3.14, and 4.19 for a rheological power-law exponent of $n = 3$.

For a relatively low value of *ak* (Figure 5a), ice follows the downhill and uphill contours of the topography, maintaining a smooth flow. As *ak* increases to 1.83 (Figure 5b), at the bottom of the trough there is a slight upward flow near the bed on the downhill side and a downward flow on the uphill side, indicating the onset of separation. As *ak* continues to rise (Figures 5c–5e), this trend becomes more pronounced. Between the bumps, four distinct regions emerge: Above the peak of the topography, the flow still exhibits the characteristic down-up motion. Below the peak, the flow in the trough reverses its direction, moving back from the stoss side of the next bump to the lee side of the previous bump (Figure 5e). This type of flow separation and re-circulation motion is studied by Gudmundsson (1997) and is also known as the Moffatt eddies that forms near sharp corners (Meyer & Creyts, 2017). Here, we show that the non-Newtonian ice flow with a power-law rheology can form such small re-circulation motion ($u < \sim 0.2$ m/year) with a smoothly varying sinusoidal basal topography.

The separation line, which marks the division of flow, is positioned slightly below the peak of the topography. In the case of $a = 100$ m, the separation line is approximately located at $z = 80$ m. The occurrence of flow separation is important because it leads to a division of the flow in the vertical direction. Hence, the presence of flow separation could hence be an indicator for the existence of an internal shear band. The upper portion of ice flows over a bed that "appears smoother" than its actual shape. Consequently, when flow separation occurs, the ice situated above the basal topography may not feel the complete underlying bed shape.

### 3.3. The Combined Effect of Topography and Rheology on Shear Band Formation

In Sections 3.1 and 3.2, we found that shear heating can dominate over advection near topographic peaks, leading to a net increase in the energy budget of basal ice. The internal shear band development depends not only on the power-law exponent *n*, but also on the shape factor of the sinusoidal topography *ak*. In this section, we aim to understand the dual effect of these two parameters and quantify their role in inducing shear localization through scaling analysis and numerical simulations.

For our scaling analysis, we consider a steady state internal shear band under a specific sinusoidal shape characterized by *ak* and rheology exponent *n*. We assume that the shear band has formed and stabilized in the flow direction, specifically we consider the pressure derivative with respect to *x* is zero. We choose the momentum equation in the *x* direction to derive the scaling relationship because ice flows primarily in the *x* direction. The momentum equation in the *x* direction can then be simplified to

$$\frac{\partial\left(2\eta\dot{e}_{xx}\right)}{\partial x} + \frac{\partial\left(2\eta\dot{e}_{xz}\right)}{\partial z} = -\rho g \sin \alpha. \tag{22}$$

We impose a generic power-law rheology without temperature dependence and assume that the main stress component is the shear stress, that is, $\tau_{II} \approx \tau_{xz}$. The viscosity has the following form

$$\eta = (2A_0)^{-\frac{1}{n}}\left(\frac{\partial u}{\partial z}\right)^{-1+\frac{1}{n}}. \tag{23}$$

For the sinusoidal topography, we choose the characteristic horizontal length *l* to be $\sim\lambda^{(n-1)p}a^{1-(n-1)p}$, where $\lambda$ is the wavelength of the bed, *p* is some constant, and *n* is the power-law exponent. We choose this exponent such that the characteristic horizontal length scale have the unit of length, and we choose $(n - 1)$ to avoid a zero denominator in the later derivation. After substituting these into the momentum equation and applying the relationship $ak = 2\pi a/\lambda$, we obtain the following

$$B_w \propto (ak)^{-2pn}. \tag{24}$$

For a more detailed derivation, please refer to Appendix E.

To test the derived scaling relationship against our simulations, we conduct four sets of numerical experiments with $n = 1, 2, 3, 4$. We include a range of shape factor *ak* values spanning from 0.52 to 6.28. A shape factor of $ak = 0.52$ corresponds to a wavelength 16 times larger than the amplitude, and $ak = 6.28$ corresponds to a scenario where the amplitude of the bump matches the wavelength. Figure 6 shows $\partial u/\partial z$ variations for different values of
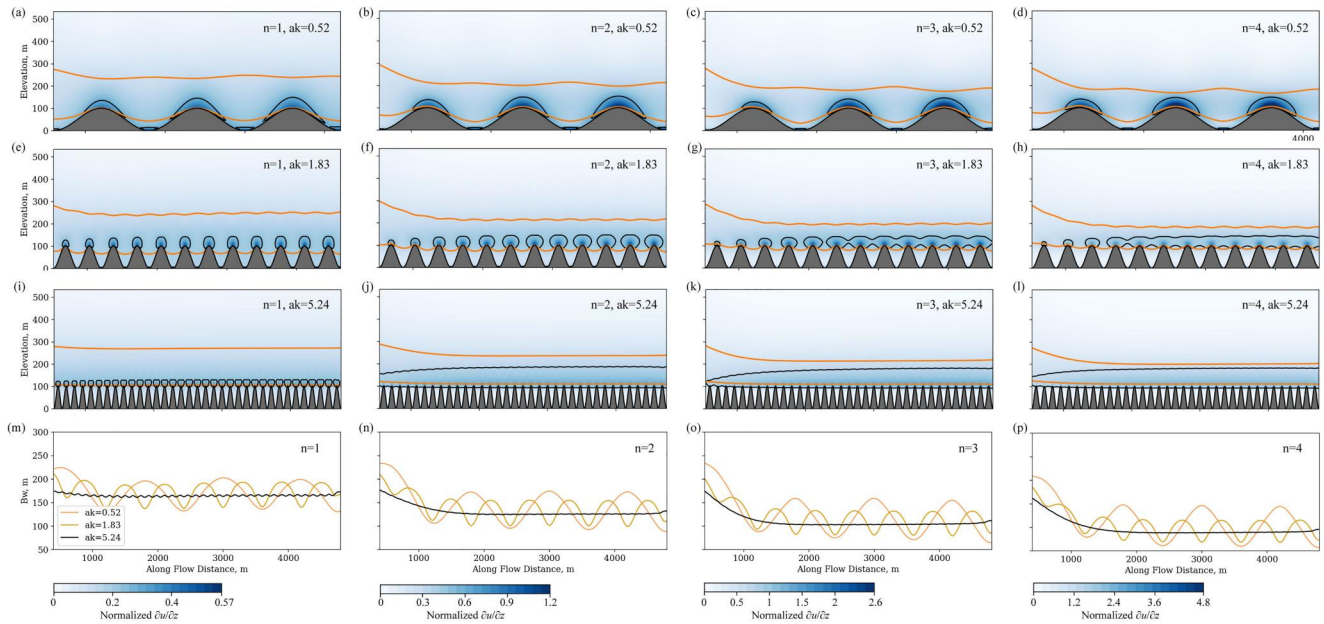
**Figure 6.** Normalized shear deformation $\partial u/\partial z$ variations for different values of the exponent $n$ and shape factor $ak$. The first three rows correspond to shape factors of $ak = 0.52$ (a–d), 1.83 (e–h), and 5.24 (i–l), respectively. Each column represents a specific value of the exponent $n$. In the first three rows of each panel, the two orange lines indicate the contours of 70% and 20%, as defined in Equation 17 and illustrated in Figure 3. The black contour in the first three rows in each panel highlights half of the maximum value of normalized $\partial u/\partial z$. The last row (m–p) shows how the thickness of the band width, defined as the vertical distance between the 70% and 20% lines, varies along the flow for different shape factors and exponents.

the exponent $n$ and shape factor $ak$. Here, we normalize the absolute value $\partial u/\partial z$ by $\bar{\dot{\epsilon}}_{xz}$, where $\bar{\dot{\epsilon}}_{xz}$ characteristic strain rate (see Equation 19), for better comparison across different $ak$ and $n$ values.

The influence of $ak$ on shear localization and shear band formation is similar across all values of $n$. When $ak$ is low (Figures 6a–6d), the shear deformation $\partial u/\partial z$ is concentrated around the topographic peaks. As $ak$ increases, the $\partial u/\partial z$ localization at the peaks begins to connect and bridge as anticipated, for example, Figures 6c, 6g, and 6k. When $ak$ is approximately 2 or larger, the shape of the $70\%u(H)$ and $20\%u(H)$ contour lines, depicted in solid orange lines in all panels, become less oscillatory and no longer align with the underlying shape of the basal topography (Figures 6j–6l). Accordingly, the band width stabilizes with fewer oscillations (Figures 6n–6p).

The relationship between $B_w/H$, $ak$, and $n$ is depicted in Figure 7. Each marker represents a normalized band width value corresponding to a specific shape factor and exponent from the simulations. To determine the stabilized band width, we compute the average band width value across three consecutive bumps in the downstream region of the domain. We exclude the upstream part from the averaging process due to the ongoing rapid thinning of the ice, which could lead to an overestimation of the band width. For cases where the $ak$ value is too small to achieve three consecutive bumps, we adjust the number of averaged bumps accordingly. The selection of the averaging area is outlined in Figures F1 and F2.

Observing the gradual increase in $ak$, we note a corresponding decreasing trend in the width of the internal shear band for all values of $n$. The rate of this decrease varies, with the slope of the log-scaled relationship approximately following a pattern of $-0.02n$. This finding suggests that for larger values of $n$, the width of the shear band decreases at a faster rate, thus enhancing the localization of the shear deformation. It is evident that as $ak$ continues to increase, the averaged band width eventually stabilizes around a certain value (Figure 7 down-triangle, cross, and up-triangle markers). This critical $ak$ value at which the width stabilizes decreases as $n$ increases. Specifically, we observe that the widths stabilize at approximately $ak = 4.45$, 3.14, 2.62 for $n = 2$, 3, 4, respectively. However, this trend is less pronounced for $n = 1$. Even at the most rugged topography considered ($ak = 6.28$), where the amplitude equals the wavelength, a stable width of the shear band is still not observed (Figure 7 circle markers).
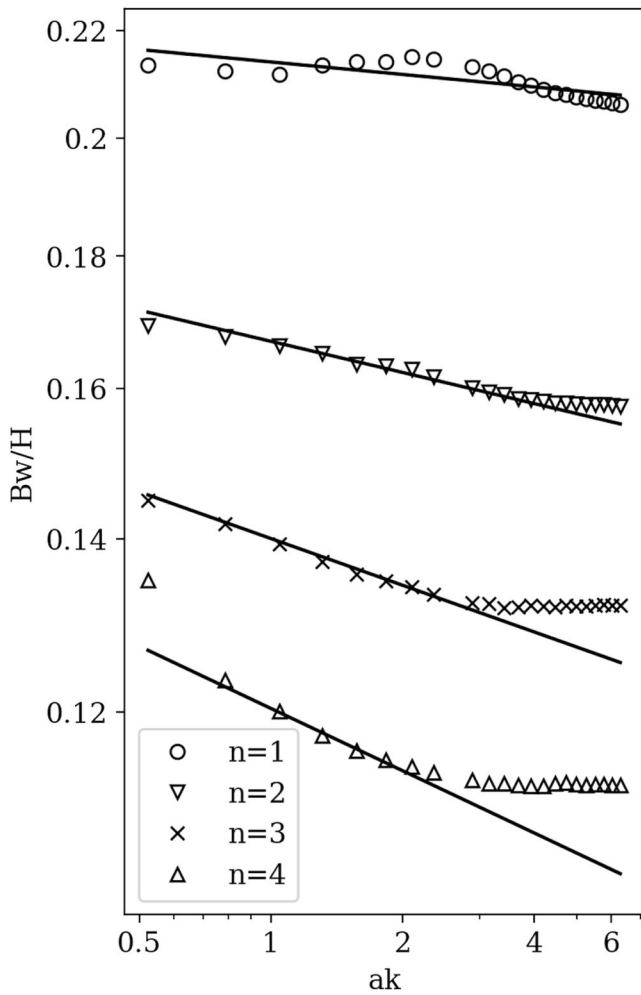
**Figure 7.** Regime diagram of the internal shear band width $B_w/H$, power-law exponent $n$, and shape factor $ak$ of the sinusoidal bed. Each marker shape corresponds to a distinct simulation set sharing the same $n$ value, and each individual marker represents a single simulation.

By varying the basal topography shape factor $ak$ and exponent $n$, we can conclude from the numerical experiments that for each exponent $n$, there exists a steady state shear band width as $ak \to \infty$ (Figure 7). When $ak$ is high, the iso-velocity-contour tend to concentrate at a consistent elevation and do not align with the shape of the basal topography (Figures F1 and F2). This result suggests that the perturbations originating from the basal topography propagate upward from the bed to the surface only over distances spanning tens to a few hundred meters, depending on the value of $n$. Thus, the influence of the actual basal topography shape on the internal ice above this level is likely reduced, and the internal ice progressively "perceives less" of the specific shapes of the basal topography.

The scaling relationship between the band width and non-dimensional shape factor $ak$ raised to the power of $-2pn$ is shown as the solid lines in Figure 7. From the simulation results, we infer that the value of $p$ is approximately 0.01. Before the width of the shear band stabilizes, the scaling of $-2pn$ captures the decreasing rate very well. Yet it is important to acknowledge that this scaling relationship does not account for the influence of temperature-dependent rheology and pressure variations in the $x$ direction. Consequently, the aforementioned relationship tends to slightly underestimate the actual degree of shear localization.

As the spacing between two bumps becomes infinitesimally small values ($ak \to \infty$), scaling suggests that $B_w$ tends toward zero, which is physically unrealistic. A zero thickness for the internal shear band implies the presence of internal "slip," where the $x$ velocity becomes discontinuous in $z$ direction. Because our model focuses on understanding shear localization, it does not permit a discontinuities in velocity anywhere in the computational domain. Hence, as $ak \to \infty$, we anticipate that $B_w$ to stabilize after surpassing a specific $ak$ value, indicating that the thickness of the internal shear band has reached its minimum possible value for a given value of $n$.

## 4. Discussion

The high speed of many glaciers and ice streams is thought to be accommodated by basal sliding, with internal deformation having only a minimal contribution (Echelmeyer & Zhongxiang, 1987; Hermann & Barclay, 1998; Rignot & Mouginot, 2012; Rignot et al., 2011). However, recent advances in our understanding of the different deformational regimes of ice particularly at high stresses (Goldsby & Kohlstedt, 2001), have led to a growing appreciation for the importance of other processes including the pronounced weakening of ice near pre-melting conditions (Krabbendam, 2016). This insight in combination with field evidence of complex, depth-dependent deformation in fast-moving ice (Hills et al., 2017; Law et al., 2023; Maier et al., 2019) merits a re-evaluation of the degree to which internal deformation may contribute to rapid ice motion.

Law et al. (2023) showed that high-resolution topography is associated with complex, depth-dependent ice flow at specific field sites in Greenland. Our study complements the work by Law et al. (2023) by providing an in-depth analysis of the two competing physical processes that govern the spontaneous, near-bed localization observed at these field sites: vertical advection and shear heating. Our simulations show that zones of intense deformation and shear heating near topographic highs link up into an internal shear band when the energy budget in the region above topographic peaks becomes positive (Figure 4). When the energy budget is negative or oscillates around a small value, shear band formation is suppressed.

Basal topography amplifies shear heating because it causes more deformation in the basal zone within the ice. This deformation is amplified by speed-up as ice is forced to wrap around topographic highs at an increasing speed, creating a positive feedback. Our analysis shows that for idealized topography, the energy budget becomes more positive as the basal topography shape factor $ak$ and the rheological power-law exponent, $n$, increases, as

shown in Figure 4. While we focus here on the power-law exponent because it is better constrained than other aspects of ice rheology such as grain-size evolution or fabric development, but these other processes could further amplify shear localization.

We emphasize that the high degree of shear localization occurring within an internal shear band can appear reminiscent of sliding at large spatial scales, but does not represent sliding. In our simulations, ice is frozen to the bed while an internal shear band forms above it, creating flow separation (Gudmundsson, 1997) between the slow-moving ice trapped in topographic troughs and the fast-moving ice above the internal shear band. As the speed-up continues, it is possible that the ice underneath the internal shear band gradually warms and becomes temperate. The existence of temperate zones with variable vertical extents depending on topography is supported by borehole data and other simulations (Harrington et al., 2015; Hills et al., 2017; Law et al., 2023).

Maier et al. (2019) drilled a network of eight boreholes in a slowly moving ridge located 33 km from the terminus of Issunguata Sermia within the ablation zone of the western margin of the Greenland Ice Sheet. Their measurements show a high shear strain rate concentrated within around 10–50 m above the bedrock, with a shear strain rate of nearly zero observed at the bedrock. Such a high localization of shear strain rate in the interior of the ice evinces the possibility of an internal sliding interface. We apply our model to match the height at which the rapid decrease in shear strain rate occurs in the borehole data ($a = 5.5$ m) and use a typical Greenland atmospheric temperature ($T_s = -12°C$). Figure 8c shows the vertical shear strain rate profile for a control run without a sinusoidal basal topography. Only Figure 8b is able to exhibit the observed drop in shear strain rate near the bed.

An important disconnect between Figures 8a–8c is the magnitude of the shear strain rate. Both of our model results show a shear strain rate that is approximately an order of magnitude higher than the observed value in order to match the surface speed of approximately 70 m/year. Figures 8d–8f show the $x$ velocity profile with depth as inferred by Maier et al. (2019) from measurements, as well as the profiles obtained from our simulations with a sine (e) and a flat (f) basal topography. Together, the panels demonstrate that our current model setup can either match the surface speed or the measured shear strain rates, but not both. The most likely explanation for this disconnect is that the observed surface speed is largely facilitated by basal sliding as sketched in Figure 8d, whereas the peak in shear strain rate may constitute the remnant of an internal shear band that may have formed upstream when ice was still flowing over a topographically variable bed.

In addition to borehole measurements of shear strain rate, our model could have important implications for the depth variability of ice fabric. For example, borehole data of grain size and cone angles collected at Siple Dome Antarctica by DiPrinzio et al. (2005) and re-analyzed by Pettit et al. (2011) reveal a localized band of ice crystals and highly oriented fabric, located several hundred meters above the bed. Several processes could contribute to the development of this ice fabric with stress being a prominent factor, as supported by shear strain rate data. However, the observed shift in fabric occurs around the depth of the Holocene transition, indicating that climate history may play an important role (Pettit et al., 2011). Despite its age, this ice fabric continues to control ice flow by partially decoupling the flow field above and below the shear band. The flow field becomes three-dimensional, potentially to the degree of eddies forming (Meyer & Creyts, 2017).

The presence of tills or other sediments underneath the ice introduces further complexity, both from a dynamic, a mechanical point of view (e.g., Hoffman & Price, 2014; King et al., 2009; MacAyeal, 1989; Minchew & Meyer, 2020) as well as a thermal point of view (e.g., Christoffersen & Tulaczyk, 2003; Rempel, 2008). One potentially interesting implication of the flow separation is that basal ice might interact in at least two distinct ways with a soft bed. One possibility is that rapid ice motion and intense shear localization could lead to warm basal ice, generating interstitial water that drains to the bed. A thick layer of temperate ice could then form in topographical lows (Law et al., 2023) and create basal melt (Karlsson et al., 2021). Alternatively, basal ice in troughs may slow down because the shear band above it accommodates most of the deformation and cools down, potentially to the degree that underlying sediments freeze into the ice, as observed by Andreassen and Winsborrow (2009).

An important limitation of our study is the assumption of a two-dimensional model along the centerline ($x$, $z$) plane of an ice stream. This assumption neglects any variations in the transverse $y$ direction, both in the ice flow and in the shape of the basal topography. In reality, the transverse flow could have a significant impact on the stress and temperature distribution, thus influencing the shear band formation. Near the shear margin, for instance, the presence of cold ice supplied from ice ridges leads to advective cooling, which counteracts viscous
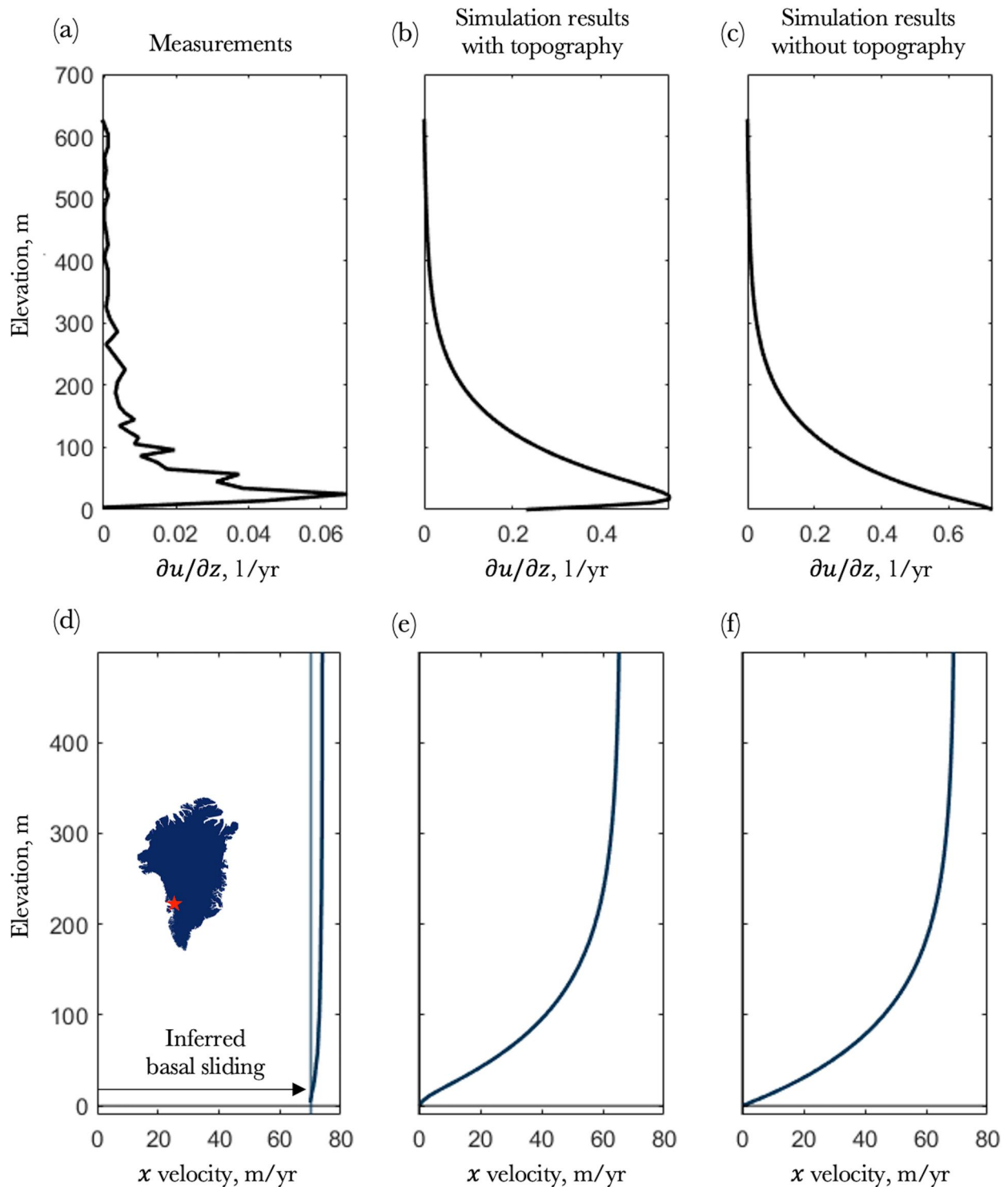
**Figure 8.** Comparison of model results against field measurements. The first column (a, d) shows the measurements at West Margin Greenland (Maier et al., 2019). The second (b, e) and third (c, f) columns show the simulation results with a flat topography and a sinusoidal topography, respectively. The first row (a–c) shows the shear strain rate $\partial u/\partial z$ distribution in the depth direction. The second row (d–f) shows the corresponding $x$ velocity profile for each case. In (d), the $x$ velocity profile is inferred by integrating the shear strain rate $\partial u/\partial z$ in (a), with the assumption of basal sliding (Maier et al., 2019). Both simulations use the power-law rheology with exponent $n = 3$. The domain extent is set as 4,800 m by 650 m. The bed height is set as 5.5 m, and surface temperature is set as −12°C. In the second and third columns, the shear strain rates and $x$ velocity profiles are obtained at $x = 4,273$ m.

heating effects (Hunter et al., 2021; Meyer & Minchew, 2018; Schoof & Mantelli, 2021; Suckale et al., 2014). Basal topography is also three-dimensional, allowing the ice not only to move up and down along the shape obstacles but also to flow around them. This lateral motion can mitigate some of the concentration of deformation that would occur exclusively at the peaks of the topography in the two-dimensional case considered herein, thus leading to a misrepresentation of the vertical structure of the velocity and stress fields (Gudmundsson, 2003; Sergienko, 2012).

## 5. Conclusion

The goal of this study is to elucidate the impact of topographically uneven bedrock on ice flow acceleration by quantifying shear localization inside the ice using numerical simulations. By incorporating sinusoidal basal topography and comparing it with a flat topography control case, we observe extensive shear localization on topographic highs, resulting in the development of an internal shear band. We analyze the impact of a power-law rheology with different exponents ($n = 1, 2, 3, 4$) and find that nonlinear rheology enhances shear heating, tilting the energy balance toward heating in the basal region of the ice. Moreover, we discover that the width of the internal shear band $B_w$ scales with the shape factor $ak$ raised to the power of $-2pn$ where $p$ is a constant. In our study, we find $p = 0.01$. This finding indicates that the development of the internal shear band is influenced by the basal topography shape. Specifically, higher values of $ak$ enhances the connection and bridging of shear deformation localization on topographical highs, hence facilitates the formation of internal shear bands. These findings contribute to our understanding of ice-sheet dynamics and provide insights for incorporating the spatial scale of the flow-to-sliding transition into ice-sheet models.

## Appendix A: Implementation of Boundary Conditions

For the outlet boundary condition, following the approach of Kreiss (1968), we estimate the propagation speed numerically by $U = \Delta x / \Delta t$, where $\Delta x$ and $\Delta t$ are the spatial and temporal grid sizes. The speed at the outlet boundary is then as follows

$$u_{n_x}^{n_t} = 2u_{n_{x-1}}^{n_{t-1}} - u_{n_{x-2}}^{n_{t-2}}, \tag{A1}$$

where $n_x$ is the boundary point and $n_t$ is the current time step.

### A1. Implementation of the Basal Interface and Free Surface

To simulate the mechanical and thermal interactions along the ice-bedrock interface, we integrate the IBM (Peskin, 1972, 2002) into the Stokes solver. The IBM is a fictitious domain method that separately discretizes the ice and rock phases with Eulerian and Lagrangian approaches. The discretization processes for each phase are independent of each other and do not require body-fitted meshes. As illustrated in Figure A1a, two sets of discretizations are used: The Lagrangian points are attached to and remain on the outline of the bed shape $\Gamma$. In contrast, the Eulerian mesh spans the entire computational domain, including the area occupied by the solid structure.

The general idea of the IBM is to solve the ice governing equations on a Eulerian grid imposed on the ice domain, $\Omega_i$, with a correction on the ice-bedrock interface $\Gamma$ at each intermediate time step to impose the boundary condition. Here, we use the direct forcing implementation of Uhlmann (2005). The implementation is decomposed into four steps. First, we advance the governing Equations 12–14 for one pseudo-time step forward without considering the submerged bedrock. We refer to this solution as the intermediate fields $u_i^{n+1/2}$ and $T^{n+1/2}$

$$\frac{u_i^{n+1/2} - u_i^n}{\Delta \mathcal{T}_u} = \left(\frac{\partial \tau_{ij}}{\partial x_j}\right)^n - \left(\frac{\partial p}{\partial x_i}\right)^n + F_i, \tag{A2}$$

$$\frac{T^{n+1/2} - T^n}{\Delta \mathcal{T}_T} = -\frac{\partial T}{\partial t} - \left(u_i\frac{\partial T}{\partial x_i}\right)^n + \frac{1}{\rho c_p}\left(\frac{\partial}{\partial x_i}\left(\kappa\frac{\partial T}{\partial x_i}\right) + 2\tau_E\dot{\epsilon}_E f(T - T_m)\right)^n, \tag{A3}$$

where the superscript $n$ represents the current pseudo-time step and $\Delta \mathcal{T}$ represents the pseudo-time step size.
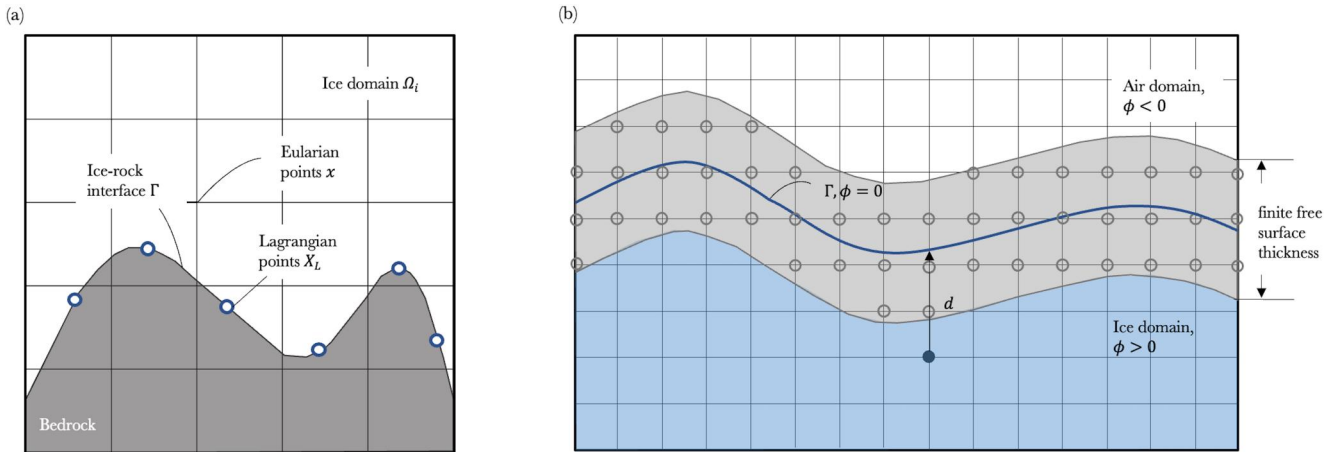
**Figure A1.** Illustration of the Immersed-Boundary Method and level-set method. (a) Treatment of the ice-bedrock interface. The spatial discretization of the ice domain $\Omega_i$ and bed shape $\Gamma$. $\Omega_i$ is discretized on a Cartesian grid $x$. The ice-bedrock interface $\Gamma$ is discretized using Lagrangian points $X_l$. (b) Treatment of the ice-air interface. The domain is divided into ice (blue) and air (white) domains using a level-set function with a finite but very small free surface thickness (light gray) of $3\Delta x$.

Second, we use a regularized delta $\delta$ function (Peskin, 2002) to translate the intermediate quantities $u_i^{n+1/2}, T^{n+1/2}$ from the Eulerian points $x$ to those on the Lagrangian points $X_l$. Dropping the superscript for simplicity, we have

$$U_i(X_l) = \sum u_i(x)\delta(x - X_l)\,\mathrm{dxdz}, \quad Q_i(X_l) = \sum q_i(x)\delta(x - X_l)\,\mathrm{dxdz}, \qquad (A4)$$

where $q_i = \partial T/\partial x_i$ denotes the heat flux, dx and dz are the horizontal and vertical grid sizes, and the lower-case and upper-case letters represent Eulerian and Lagrangian quantities, respectively. The delta function is a continuous differentiable function that takes 1 if the Eulerian grid point is on the Lagrangian point and 0 if the Eulerian grid point is far away, thus allowing a smooth transfer between the grids.

Third, we compute the volume forces $F_{U_i}$ and $F_{Q_i}$ required to achieve the desired boundary conditions, which are, in this case, the no-slip condition $U_x^d = U_z^d = 0$ and constant geothermal heating condition $Q_i^d$

$$\frac{U_i^{n+1/2} - U_i^d}{\Delta\mathcal{T}_u} = F_{U_i}^{n+1/2}, \quad \frac{Q_i^{n+1/2} - Q_i^d}{\Delta\mathcal{T}_T} = F_{Q_i}^{n+1/2}. \qquad (A5)$$

Finally, we use the computed volume force to correct the intermediate fields $u$ and $T$ and obtain the velocity and temperature fields at the next pseudo-time step

$$u_i^{n+1} = u_i^{n+1/2} + \frac{F_{U_i}^{n+1/2}}{\Delta V_{\mathrm{lag}}}\Delta\mathcal{T}_u, \quad q_i^{n+1} = q_i^{n+1/2} + \frac{F_{Q_i}^{n+1/2}}{\Delta V_{\mathrm{lag}}}\Delta\mathcal{T}_T, \qquad (A6)$$

where $\Delta V_{\mathrm{lag}}$ is the control volume of one Lagrangian point. In our model, we select the number of Lagrangian points such that $\Delta V_{\mathrm{lag}} \sim \mathrm{dxdz}$.

The other interface that requires careful numerical treatment is the upper surface of the ice. Ice thins as it speeds up and the free surface moves downward toward the bed. While the movement itself is relatively slow and gradual, its thermal implications could be very important (e.g., Mantelli et al., 2019). To capture ice thinning, we represent the free surface as the level-set of a higher dimensional distance function, as illustrated in Figure A1b, allowing us to implicitly handle the moving front as discussed in the books by Sethian (1999, Chapter 2) and Osher et al. (2004, Chapter 2). More specifically, the ice-air interface is defined as the zero-contour of a signed distance function $\phi$

$$\phi(x) = \begin{cases} -d & \text{if } x \in \text{ air,} \\ +d & \text{if } x \in \text{ ice,} \\ 0 & \text{if } x \in \Gamma, \end{cases} \tag{A7}$$

where $d$ is the distance from the grid point to the interface. Across $\phi(x) = 0$, the density $\rho$, viscosity $\eta$, and thermal conductivity $\kappa$ change

$$\rho(\phi) = \rho_a + (\rho_i - \rho_a) H(\phi), \tag{A8}$$

$$\eta(\phi) = \eta_a + (\eta_i - \eta_a) H(\phi), \tag{A9}$$

$$\kappa(\phi) = \kappa_a + (\kappa_i - \kappa_a) H(\phi), \tag{A10}$$

where the subscript $i$ and $a$ denote the material properties in the ice and the air domain, respectively. $H$ is the Heaviside function defined as

$$H(\phi) = \begin{cases} 0 & \phi < -\epsilon, \\ \frac{1}{2} + \frac{\phi}{2\epsilon} + \frac{1}{2\pi} \sin \frac{\pi\phi}{\epsilon} & -\epsilon \leq \phi \leq \epsilon, \\ 1 & \phi > \epsilon, \end{cases} \tag{A11}$$

with a smoothing length of $\epsilon = 3\Delta x$.

To evolve the location of the interface, we advect the level field using the general advection equation, also known as the level-set equation

$$\frac{\partial \phi}{\partial t} + u_n |\nabla \phi| = 0, \tag{A12}$$

where $u_n$ is the physical velocity in direction normal to the ice surface. This equation moves the implicit front with the ice velocity field determined by the mechanical Equation 2 at each physical time step. The spatial discretizations use first-order upwind and the temporal discretizations use the second-order accurate Total Variation Diminishing Runge–Kutta schemes. Because the ice-air interface remains smooth at all times and thins only slightly as compared to the overall thickness of the ice sheet, sophisticated advection schemes such as extension velocities (Adalsteinsson & Sethian, 1999), topology-preservation techniques (Qin et al., 2015), or re-initialization (Osher et al., 2004) are not necessary in our case.

We performed two test cases, circular inclusion and Nye's problem, to verify our numerical approach. The details of the test cases can be found in Appendix B.

## Appendix B: Verification

To verify the accuracy of our numerical method, we compare our simulations to two analytical solutions: the circular inclusion test (Schmid & Podladchikov, 2003) and the classic Nye solution for the velocity field in ice flowing over a wavy surface (Nye, 1969). These two benchmarks are complementary. The circular inclusion test is valuable for identifying spurious oscillations in the pressure field whereas the Nye solution represents a flow configuration that is more closely related to the dynamic problem we aim to understand.

Following Schmid and Podladchikov (2003), we consider a circular solid inclusion immersed in a square domain with homogeneous fluid. We apply a pure shear boundary condition to the outside of the fluid domain and a no-slip condition to the inclusion-fluid boundary. To evaluate the accuracy of the numerical scheme, we compare our numerical results to the analytical solutions for the pressure and velocity fields
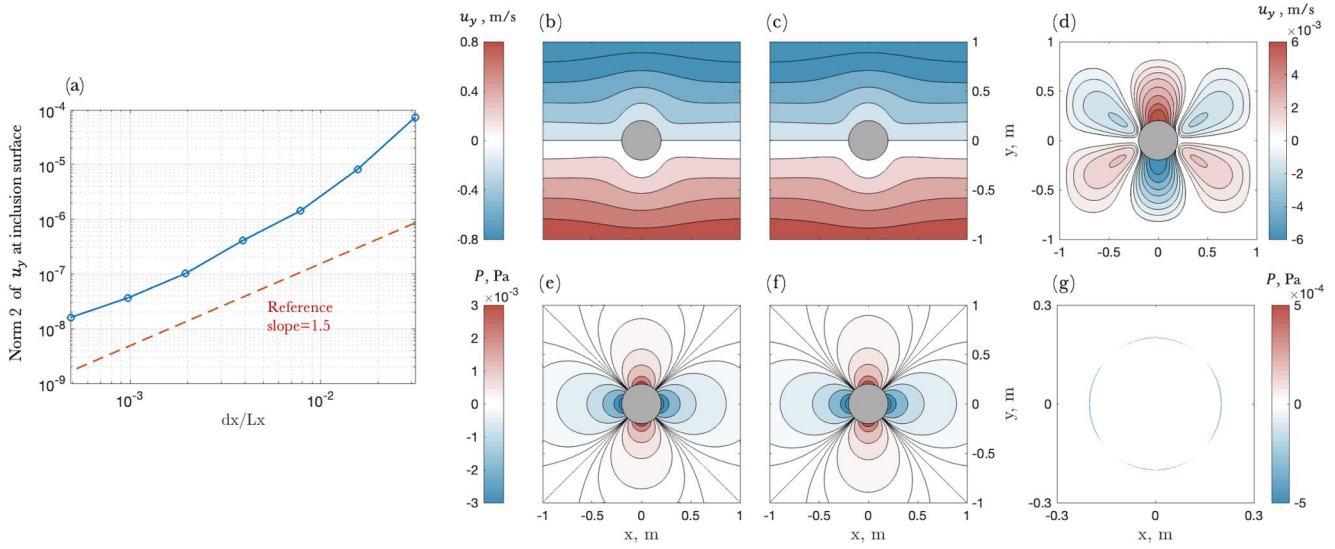
**Figure B1.** Comparison of numerical solutions against analytical solutions of the inclusion problem. (a) L2 norm of the vertical velocity $u_y$ at the cylinder boundary. (b–d) Vertical velocity $u_y$ for the analytical and numerical cases and their difference, respectively. The black solid lines in (b) and (c) represent the streamlines. (e–g) Pressure distribution for the analytical and numerical cases and their difference, respectively. The spatial resolution shown here is $512 \times 512$ grid cells in the $x$ and $y$ directions.

$$v_x + iv_y = \epsilon R^2\left(-\frac{1}{z} - \frac{z^3}{r^4} + R^2\frac{z^3}{r^6}\right) + \dot{\epsilon}\frac{r^2}{z}, \tag{B1}$$

$$P = 4\eta\epsilon\cos(2\theta)\frac{R^2}{r^2}, \tag{B2}$$

where $z = x + iy = re^{i\theta}$, $\epsilon$ is the shear strain rate, $\eta$ is the fluid viscosity and $R$ is the radius of the inclusion. The applied boundary conditions are the pure shear as follows

$$v_x = \dot{\epsilon}x, v_y = -\dot{\epsilon}y. \tag{B3}$$

Figure B1 summarizes the results of our benchmark comparison for the inclusion case. Panel (a) shows the spatial convergence test, indicating that the combination of our Stokes solver and IBM leads to a spatial convergence rate of about 1.5. Panels (b–d) compare the numerical and the analytical solutions for the vertical velocity and their difference. Panels (e–g) compare the numerical and the analytical solutions for the pressure and their difference. Our numerical method shows satisfactory agreement with the analytical solution.

To test our model against Nye's asymptotic analysis of a viscous Newtonian fluid flowing over a wavy bed, we follow the model setting of Nye (1969) and impose a sine wave at the bed, $z_0 = \epsilon a\sin(kx)$. The boundary conditions are $(\tau_x, \tau_z) = (1, 0)$ on the surface and periodic in the flow direction. We limit our reference analytical solution to only first order $\mathcal{O}(\epsilon)$

$$u = U\big(1 + z\epsilon a\beta k^2\exp(-kz)\sin(kx)\big) + \mathcal{O}(\epsilon^2), \tag{B4}$$

$$v = U\epsilon a\beta k(1 + kz)\exp(-kz)\cos(kx) + \mathcal{O}(\epsilon^2), \tag{B5}$$

$$p = 2\epsilon\eta Ua\beta k^2\exp(-kz)\cos(kx) + \mathcal{O}(\epsilon^2), \tag{B6}$$

where $U$ is the far field horizontal velocity, $\beta = k_*^2/(k_*^2 + k^2)$, and $k_*$ denotes the characteristic wavenumber of regelation. The full solution can be found in Nye (1969). We choose $U = 1$ m/year, $\epsilon = 1$, $a = 1$ m, $\eta = 1$ bar year, $k = 1$ m$^{-1}$, and $k_* = 0.6$ m$^{-1}$. The physical domain is $50\pi$ m by $20\pi$ m.
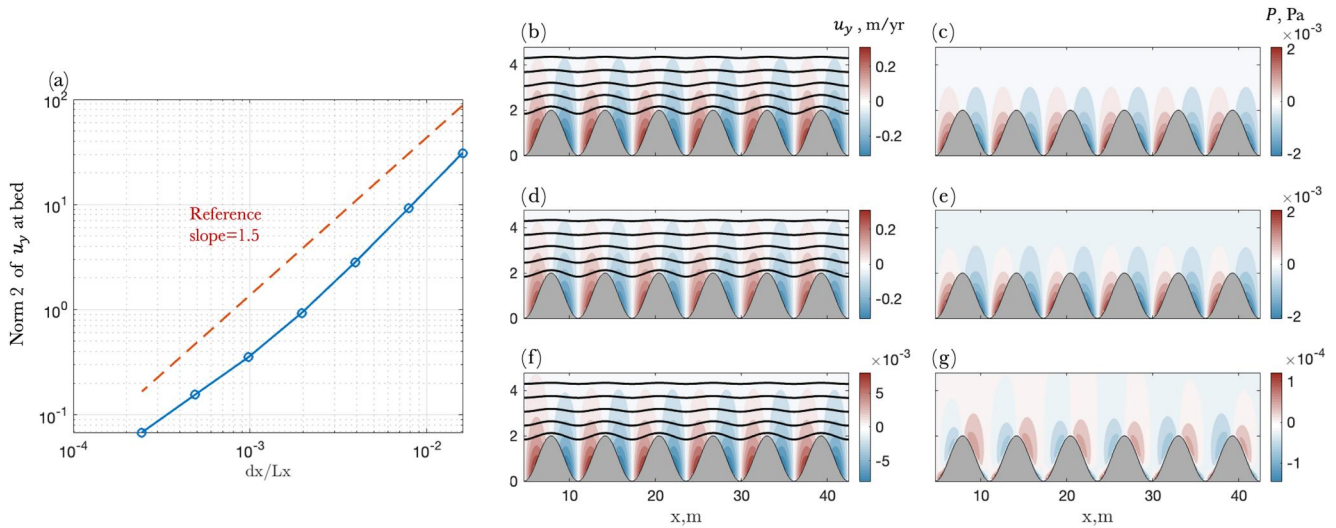
**Figure B2.** Comparison of numerical solutions against analytical solutions of Nye's problem. (a) L2 norm of the vertical component of velocity $u_y$ at the bed. (b, d, f) Vertical velocity for the analytical and numerical cases and their difference, respectively. The black solid lines represent the streamlines. (c, e, g) Pressure distribution for the analytical and numerical cases and their difference, respectively. The spatial resolution shown here is $512 \times 128$ grid cells in the $x$ and $z$ directions.

Figure B2 summarizes the results from our comparison with Nye (1969). Panel (a) shows that the convergence rate of our numerical approach is around 1.5. Panels (b, d, f) show a comparison between the numerical and analytical solutions for the vertical velocity and their difference. Panels (c, e, g) show a comparison between the numerical and analytical solutions for the pressure and their difference. Overall, our numerical method shows satisfactory agreement with the analytical solution.

## Appendix C: Example Simulation Results of Ice Surface Evolution

We show one example of ice surface evolution over time in Figure C1 using the model described in Section 2. Here, we use a flat basal topography and simulate the ice flow over 80 years. At the scale of the computational domain, the ice surface change is not immediately apparent.
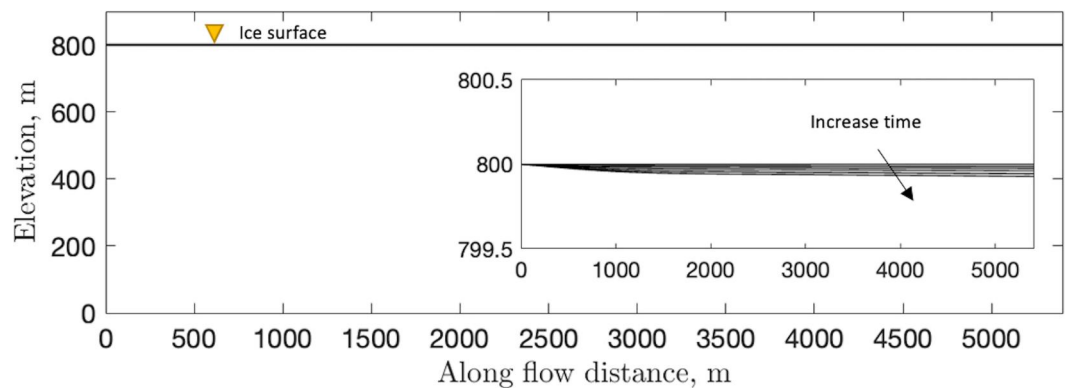


**Figure C1.** Ice surface evolution over 80 years on a flat bed. The sub-panel shows a zoom-in view of the ice surface evolution.

## Appendix D: Scaling of the Energy Equation

To identify the relative magnitude of the terms in the energy Equation 11, we perform a scaling analysis. We choose the characteristic parameters as follows

$$\bar{z} = H, \ \bar{\tau} = \rho g H \alpha, \ \bar{u} = \bar{U}_s = \frac{2(\rho g \alpha)^n A_0}{n+1} H^{n+1}, \ \bar{T} = T_s, \tag{D1}$$

where $H = 1{,}000$ m is the characteristic ice thickness, $a = 100$ m is the characteristic bed height, $T_s = -26°C$ is a typical atmospheric temperature in Antarctica, and $\alpha = 2°$ is the characteristic bed slope. Other relevant constants include the specific heat of ice $c_p = 2{,}096.9$ J/(kg · K), ice density $\rho = 900$ kg/m$^3$, and thermal conductivity $\kappa = 2.51$ W/(m · K).

In this study, we define the internal shear band to be a zone where half of the total ice deformation occurs in the ice column. Therefore, the characteristic shear strain rate is calculated as half of the characteristic speed divided by the characteristic vertical scale. This vertical scale will be the thickness of the boundary layer, which is the internal shear band thickness $B_w$ (Equation 19) in our case. The expression for characteristic shear strain rate is then

$$\bar{\dot{\epsilon}}_{xz} = \frac{0.5 \bar{U}_s}{B_w} = \frac{(\rho g \alpha)^n A_0}{B_w (n+1)} H^{n+1}. \tag{D2}$$

For the characteristic vertical speed (or thinning speed), we assume that $U_t \sim \bar{U}_s \times 10^{-2} - 10^{-3}$ and $B_w \sim 50$–$500$ m. By substituting in the characteristic values and the constants, we obtain the scaling of the spatial terms

$$\rho c_p \left( u_i \frac{\partial T}{\partial x_i} \right) \sim \mathcal{O}(10^{-3}), \ \ \frac{\partial}{\partial x_i} \left( \kappa \frac{\partial T}{\partial x_i} \right) \sim \mathcal{O}(10^{-5}), \ 2\tau_E \dot{\epsilon}_E \sim \mathcal{O}(10^{-3}). \tag{D3}$$

Note that in our problem setting of an ice slab flowing down a slope, the dominant strain rate is the shear strain rate $\dot{\epsilon}_{xz}$, and the dominant advection is the vertical advection $U_t (\partial T / \partial z)$.

## Appendix E: Scaling of the Momentum Equation

We assume a generic power-law rheology without temperature dependence,

$$\dot{\epsilon}_{ij} = A \tau_{II}^{n-1} \tau_{ij}, \ \tau_{ij} = 2\eta \dot{\epsilon}_{ij}. \tag{E1}$$

The viscosity can be expressed as

$$\eta = (2A_0)^{-\frac{1}{n}} \left( 2\dot{\epsilon}_{xx}^2 + 2\dot{\epsilon}_{zz}^2 + 4\dot{\epsilon}_{xz}^2 \right)^{\frac{1-n}{2n}}. \tag{E2}$$

We assume the dominant strain rate is the shear strain rate in the shear band, thus the square of strain rates in other directions can be ignored. We also assume that horizontal gradients of the vertical velocity are small compared to the vertical gradient of the horizontal velocity, or $\partial w / \partial x \ll \partial u / \partial z$. The viscosity is then simplified to

$$\eta = (2A_0)^{-\frac{1}{n}} \left( \frac{\partial u}{\partial z} \right)^{\frac{1-n}{n}}. \tag{E3}$$

Upon substitution of the viscosity, the $x$ momentum Equation 22 is

$$2\eta \frac{\partial^2 u}{\partial x^2} + \frac{1}{n} \eta \frac{\partial^2 u}{\partial z^2} = \rho g \alpha, \tag{E4}$$

$$2 \frac{\partial^2 u}{\partial x^2} + \frac{1}{n} \frac{\partial^2 u}{\partial z^2} = (2A_0)^{\frac{1}{n}} \left( \frac{\partial u}{\partial z} \right)^{1-\frac{1}{n}} \rho g \alpha. \tag{E5}$$

It is important to note that the second derivative of $x$ velocity is not necessarily negligible. We assume a characteristic horizontal length of $l$. For the sinusoidal topography, we consider $l$ to be $\sim \lambda^{(n-1)p} a^{1-(n-1)p}$, where $\lambda$ is

the wavelength, $p$ is a constant, and $n$ is the power-law exponent. We choose $(n-1)$ to avoid a zero denominator in the later derivation. Finally the $x$ momentum equation can be expressed as follows

$$\left(\frac{2}{l^2} + \frac{1}{n}\frac{1}{B_w^2}\right) = D\frac{1}{B_w^{1-\frac{1}{n}}}, \tag{E6}$$

where $D = \rho g \alpha (2A_0)^{\frac{1}{n}} u^{-\frac{1}{n}}$. By simplifying the equation, we obtain the following relationship

$$l^2 = \frac{2nB_w^2}{DnB_w^{\frac{1}{n}+1} - 1}. \tag{E7}$$

By substituting representative values of $\rho = 900$ kg/m$^3$, $g = 9.8$ m/s$^2$, $\alpha \sim 1°$–$5°$, $A_0 \sim 10^{-12}$ Pa$^{-1}$ s$^{-1}$– $10^{-29}$ Pa$^{-4}$ s$^{-1}$, $u \sim 50$–$100$ m/year, and $B_w \sim 50$–$500$ m, we have $DnB_w^{\frac{1}{n}+1} \sim 10^1 - 10^2$, thus the relationship between $l$ and $B_w$ can be further approximated to the following form

$$l^2 = \frac{2nB_w^2}{DnB_w^{\frac{1}{n}+1}}, \tag{E8}$$

$$B_w \propto l^{\frac{2n}{n-1}}. \tag{E9}$$

By substituting $ak = 2\pi a/\lambda$, we can also express the above relationship as follows

$$B_w \propto (ak)^{-2pn}. \tag{E10}$$

## Appendix F: $x$ Velocity Ratio Distribution for Different $n$ Values and Topographies

Figures F1 and F2 depict contour lines ranging from 15% to 95% of the surface $x$ velocity, with each contour line spaced by 3%. When $ak$ is low, the $x$ velocity ratio contours exhibit a higher concentration around the peak region and a relatively more evenly spaced distribution around the trough. This behavior indicates that the ice experiences vertical compression and extension as it flows over the basal topography. Furthermore, this observation suggests that the perturbations originating from the basal topography propagate upward from the bed to the surface over distances spanning tens to several hundreds of meters. In contrast, when $ak$ is high, the $x$ velocity ratio contours tend to concentrate at a consistent elevation and do not align with the shape of the basal topography. Thus, the ice no longer experiences the alternation between vertical compression and extension as flows downstream. This outcome implies that the actual form of the basal topography exerts significantly less influence on the internal ice, and the flow becomes considerably detached from the true shape of the basal topography.
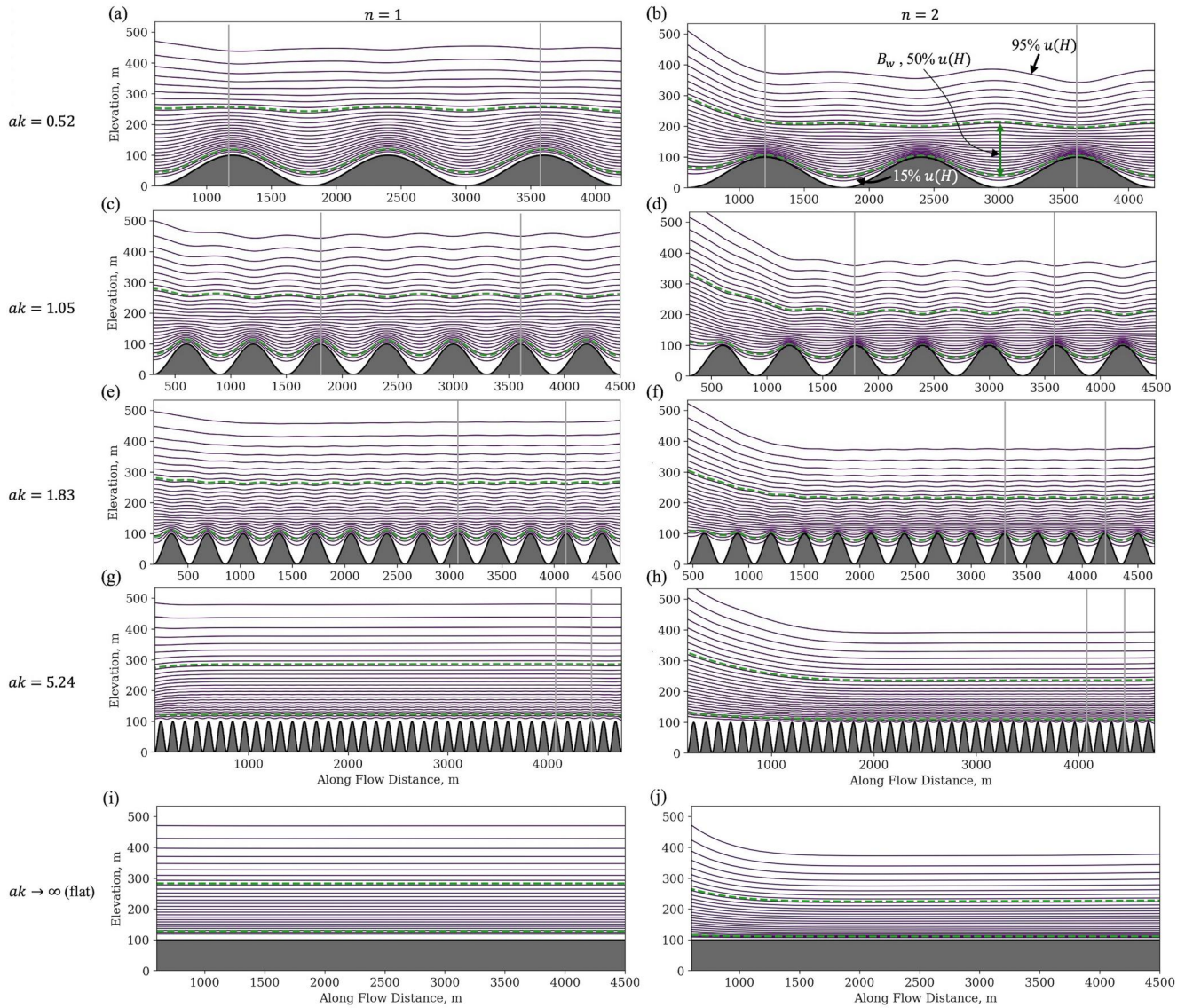
**Figure F1.** $x$ velocity ratio (local $x$ velocity divided by the surface $x$ velocity in the same ice column) contours for $n = 1$, 2 and different values of $ak$. Each row corresponds to a different shape factor: $ak = 0.52$, 1.05, 1.83, 5.24, and $\infty$ (representing a flat bed). The first and second columns represent the case where $n = 1$ and $n = 2$, respectively. In each panel, the purple lines represent the contour lines from 95% to 15%, with a separation of 3%. The two green dashed lines represent the contour lines of 70% and 20%, which define the upper and lower bounds of the internal shear band. Gray vertical lines indicate the spatial $x$ locations where we calculate the average internal shear band width.
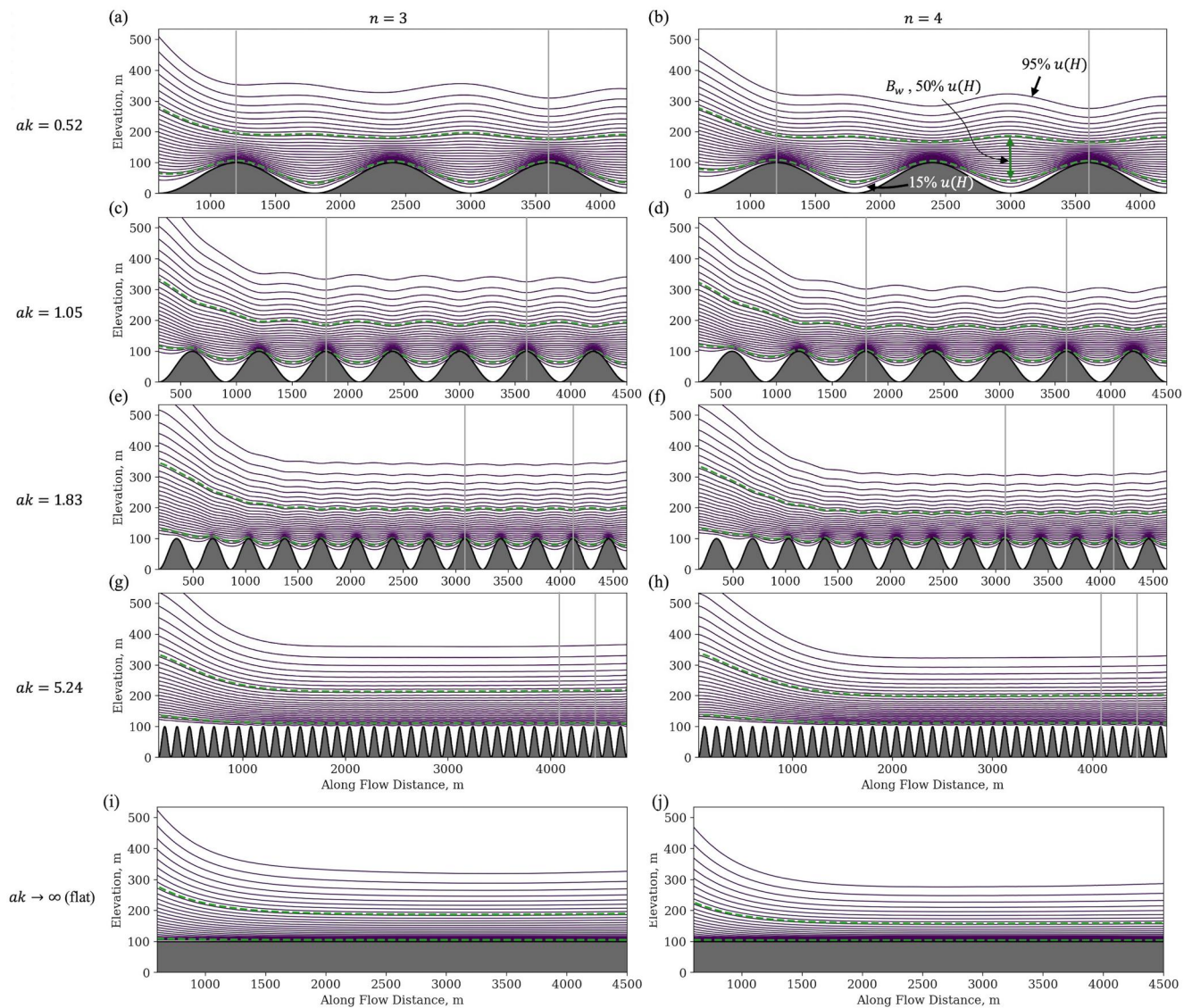
**Figure F2.** The $x$ velocity ratio contours for different values of $n = 3$, 4 and different $ak$. The layout of this figure is the same as in Figure F1.

## Data Availability Statement

## References

Adalsteinsson, D., & Sethian, J. A. (1999). The fast construction of extension velocities in level set methods. *Journal of Computational Physics*, *148*(1), 2–22. https://doi.org/10.1006/jcph.1998.6090

Adams, C. J., Iverson, N. R., Helanow, C., Zoet, L. K., & Bate, C. E. (2021). Softening of temperate ice by interstitial water. *Frontiers in Earth Science*, *9*, 702761. https://doi.org/10.3389/feart.2021.702761

Andreassen, K., & Winsborrow, M. (2009). Signature of ice streaming in bjørnøyrenna, polar north Atlantic, through the Pleistocene and implications for ice-stream dynamics. *Annals of Glaciology*, *50*(52), 17–26. https://doi.org/10.3189/172756409789624238

Barnes, P., Tabor, D., & Walker, J. (1971). The friction and creep of polycrystalline ice. *Proceedings of the Royal Society of London. A. Mathematical and Physical Sciences*, *324*(1557), 127–155.

Bons, P. D., Kleiner, T., Llorens, M.-G., Prior, D. J., Sachau, T., Weikusat, I., & Jansen, D. (2018). Greenland ice sheet: Higher nonlinearity of ice flow significantly reduces estimated basal motion. *Geophysical Research Letters*, *45*(13), 6542–6548. https://doi.org/10.1029/2018gl078356

Bueler, E., & Brown, J. (2009). Shallow shelf approximation as a "sliding law" in a thermomechanically coupled ice sheet model. *Journal of Geophysical Research*, *114*(F3), F03008. https://doi.org/10.1029/2008jf001179

Carsey, F., Behar, A., Lane, A. L., Realmuto, V., & Engelhardt, H. (2002). A borehole camera system for imaging the deep interior of ice sheets. *Journal of Glaciology*, *48*(163), 622–628. https://doi.org/10.3189/172756502781831124

Christoffersen, P., & Tulaczyk, S. (2003). Thermodynamics of basal freeze-on: Predicting basal and subglacial signatures of stopped ice streams and interstream ridges. *Annals of Glaciology*, *36*, 233–243. https://doi.org/10.3189/172756403781816211

Clarke, G. K. (1987). Fast glacier flow: Ice streams, surging, and tidewater glaciers. *Journal of Geophysical Research*, *92*(B9), 8835–8841. https://doi.org/10.1029/jb092ib09p08835

Clarke, G. K., Nitsan, U., & Paterson, W. (1977). Strain heating and creep instability in glaciers and ice sheets. *Reviews of Geophysics*, *15*(2), 235–247. https://doi.org/10.1029/rg015i002p00235

DiPrinzio, C., Wilen, L. A., Alley, R., Fitzpatrick, J., Spencer, M., & Gow, A. (2005). Fabric and texture at siple dome, Antarctica. *Journal of Glaciology*, *51*(173), 281–290. https://doi.org/10.3189/172756505781829359

Doyle, S. H., Hubbard, B., Christoffersen, P., Young, T. J., Hofstede, C., Bougamont, M., et al. (2018). Physical conditions of fast glacier flow: 1. Measurements from boreholes drilled to the bed of Store Glacier, west Greenland. *Journal of Geophysical Research: Earth Surface*, *123*(2), 324–348. https://doi.org/10.1002/2017jf004529

Echelmeyer, K., & Zhongxiang, W. (1987). Direct observation of basal sliding and deformation of basal drift at sub-freezing temperatures. *Journal of Glaciology*, *33*(113), 83–98. https://doi.org/10.3189/s0022143000005396

Fowler, A. C. (2001). Modelling the flow of glaciers and ice sheets. In *Continuum mechanics and applications in geophysics and the environment* (pp. 201–221). Springer.

Glen, J. W. (1955). The creep of polycrystalline ice. *Proceedings of the Royal Society of London. A. Mathematical and Physical Sciences*, *228*(1175), 519–538.

Glen, J. W. (1952). Experiments on the deformation of ice. *Journal of Glaciology*, *2*(12), 111–114. https://doi.org/10.1017/s0022143000034067

Goldsby, D., & Kohlstedt, D. L. (2001). Superplastic deformation of ice: Experimental observations. *Journal of Geophysical Research*, *106*(B6), 11017–11030. https://doi.org/10.1029/2000jb900336

Goodwin, I. D. (1993). Basal ice accretion and debris entrainment within the coastal ice margin, law dome, Antarctica. *Journal of Glaciology*, *39*(131), 157–166. https://doi.org/10.1017/s002214300001580x

Gow, A., Epstein, S., & Sheehy, W. (1979). On the origin of stratified debris in ice cores from the bottom of the Antarctic ice sheet. *Journal of Glaciology*, *23*(89), 185–192. https://doi.org/10.1017/s0022143000029828

Gudmundsson, G. H. (1997). Basal-flow characteristics of a non-linear flow sliding frictionless over strongly undulating bedrock. *Journal of Glaciology*, *43*(143), 80–89. https://doi.org/10.1017/s0022143000002835

Gudmundsson, G. H. (2003). Transmission of basal variability to a glacier surface. *Journal of Geophysical Research*, *108*(B5), 2253. https://doi.org/10.1029/2002jb002107

Harrington, J. A., Humphrey, N. F., & Harper, J. T. (2015). Temperature distribution and thermal anomalies along a flowline of the Greenland ice sheet. *Annals of Glaciology*, *56*(70), 98–104. https://doi.org/10.3189/2015aog70a945

Helanow, C., Iverson, N. R., Woodard, J. B., & Zoet, L. K. (2021). A slip law for hard-bedded glaciers derived from observed bed topography. *Science Advances*, *7*(20), eabe7798. https://doi.org/10.1126/sciadv.abe7798

Helanow, C., Iverson, N. R., Zoet, L. K., & Gagliardini, O. (2020). Sliding relations for glacier slip with cavities over three-dimensional beds. *Geophysical Research Letters*, *47*(3), e2019GL084924. https://doi.org/10.1029/2019gl084924

Hermann, E., & Barclay, K. (1998). Basal sliding of ice stream B, west Antarctica. *Journal of Glaciology*, *44*(147), 223–230. https://doi.org/10.3189/s0022143000002562

Herron, S., & Langway, C. C. (1979). The debris-laden ice at the bottom of the Greenland ice sheet. *Journal of Glaciology*, *23*(89), 193–207. https://doi.org/10.3189/s002214300002983x

Hills, B. H., Harper, J. T., Humphrey, N. F., & Meierbachtol, T. W. (2017). Measured horizontal temperature gradients constrain heat transfer mechanisms in Greenland ice. *Geophysical Research Letters*, *44*(19), 9778–9785. https://doi.org/10.1002/2017gl074917

Hoffman, M., & Price, S. (2014). Feedbacks between coupled subglacial hydrology and glacier dynamics. *Journal of Geophysical Research: Earth Surface*, *119*(3), 414–436. https://doi.org/10.1002/2013jf002943

Hunter, P., Meyer, C., Minchew, B., Haseloff, M., & Rempel, A. (2021). Thermal controls on ice stream shear margins. *Journal of Glaciology*, *67*(263), 435–449. https://doi.org/10.1017/jog.2020.118

Joughin, I., Rignot, E., Rosanova, C. E., Lucchitta, B. K., & Bohlander, J. (2003). Timing of recent accelerations of pine island glacier, Antarctica. *Geophysical Research Letters*, *30*(13), 39-1. https://doi.org/10.1029/2003gl017609

Joughin, I., Smith, B. E., Howat, I. M., Scambos, T., & Moon, T. (2010). Greenland flow variability from ice-sheet-wide velocity mapping. *Journal of Glaciology*, *56*(197), 415–430. https://doi.org/10.3189/002214310792447734

Karlsson, N. B., Solgaard, A. M., Mankoff, K. D., Gillet-Chaulet, F., MacGregor, J. A., Box, J. E., et al. (2021). A first constraint on basal meltwater production of the Greenland ice sheet. *Nature Communications*, *12*(1), 3461. https://doi.org/10.1038/s41467-021-23739-z

King, E. C., Hindmarsh, R. C., & Stokes, C. (2009). Formation of mega-scale glacial lineations observed beneath a west Antarctic ice stream. *Nature Geoscience*, *2*(8), 585–588. https://doi.org/10.1038/ngeo581

Krabbendam, M. (2016). Sliding of temperate basal ice on a rough, hard bed: Creep mechanisms, pressure melting, and implications for ice streaming. *The Cryosphere*, *10*(5), 1915–1932. https://doi.org/10.5194/tc-10-1915-2016

Kreiss, H.-O. (1968). Stability theory for difference approximations of mixed initial boundary value problems. I. *Mathematics of Computation*, *22*(104), 703–714. https://doi.org/10.2307/2004572

Larson, F. (1980). The uniqueness of steady state flows of glaciers and ice sheets. *Geophysical Journal International*, *63*(2), 333–345. https://doi.org/10.1111/j.1365-246x.1980.tb02624.x

Law, R., Christoffersen, P., MacKie, E., Cook, S., Haseloff, M., & Gagliardini, O. (2023). Complex motion of Greenland ice sheet outlet glaciers with basal temperate ice. *Science Advances*, *9*(6), eabq5180. https://doi.org/10.1126/sciadv.abq5180

Lüthi, M., Funk, M., Iken, A., Gogineni, S., & Truffer, M. (2002). Mechanisms of fast flow in Jakobshavn Isbræ, west Greenland: Part III. Measurements of ice deformation, temperature and cross-borehole conductivity in boreholes to the bedrock. *Journal of Glaciology*, *48*(162), 369–385. https://doi.org/10.3189/172756502781831322

MacAyeal, D. R. (1989). Large-scale ice flow over a viscous basal sediment: Theory and application to ice stream b, Antarctica. *Journal of Geophysical Research*, *94*(B4), 4071–4087. https://doi.org/10.1029/jb094ib04p04071

Maier, N., Humphrey, N., Harper, J., & Meierbachtol, T. (2019). Sliding dominates slow-flowing margin regions, Greenland ice sheet. *Science Advances*, *5*(7), eaaw5406. https://doi.org/10.1126/sciadv.aaw5406

Mantelli, E., Haseloff, M., & Schoof, C. (2019). Ice sheet flow with thermally activated sliding. Part 1: The role of advection. *Proceedings of the Royal Society A*, *475*(2230), 20190410. https://doi.org/10.1098/rspa.2019.0410

Maule, C. F., Purucker, M. E., Olsen, N., & Mosegaard, K. (2005). Heat flux anomalies in Antarctica revealed by satellite magnetic data. *Science*, *309*(5733), 464–467. https://doi.org/10.1126/science.1106888

Mellor, M., & Testa, R. (1969). Effect of temperature on the creep of ice. *Journal of Glaciology*, *8*(52), 131–145. https://doi.org/10.1017/s0022143000020803

Meyer, C. R., & Creyts, T. T. (2017). Formation of ice eddies in subglacial mountain valleys. *Journal of Geophysical Research: Earth Surface*, *122*(9), 1574–1588. https://doi.org/10.1002/2017jf004329

Meyer, C. R., & Minchew, B. M. (2018). Temperate ice in the shear margins of the Antarctic ice sheet: Controlling processes and preliminary locations. *Earth and Planetary Science Letters*, *498*, 17–26. https://doi.org/10.1016/j.epsl.2018.06.028

Millstein, J. D., Minchew, B. M., & Pegler, S. S. (2022). Ice viscosity is more sensitive to stress than commonly assumed. *Communications Earth & Environment*, *3*(1), 57. https://doi.org/10.1038/s43247-022-00385-x

Minchew, B. M., & Meyer, C. R. (2020). Dilation of subglacial sediment governs incipient surge motion in glaciers with deformable beds. *Proceedings of the Royal Society A*, *476*(2238), 20200033. https://doi.org/10.1098/rspa.2020.0033

Morlighem, M., Williams, C. N., Rignot, E., An, L., Arndt, J. E., Bamber, J. L., et al. (2017). Bedmachine v3: Complete bed topography and ocean bathymetry mapping of Greenland from multibeam echo sounding combined with mass conservation. *Geophysical Research Letters*, *44*(21), 11–051. https://doi.org/10.1002/2017gl074954

Mouginot, J., Rignot, E., & Scheuchl, B. (2014). Sustained increase in ice discharge from the Amundsen Sea embayment, west Antarctica, from 1973 to 2013. *Geophysical Research Letters*, *41*(5), 1576–1584. https://doi.org/10.1002/2013gl059069

Nye, J. F. (1969). A calculation on the sliding of ice over a wavy surface using a Newtonian viscous approximation. *Proceedings of the Royal Society of London. A. Mathematical and Physical Sciences*, *311*(1506), 445–467.

Nye, J. F. (1971). Causes and mechanics of glacier surges: Discussion. *Canadian Journal of Earth Sciences*, *8*(2), 306–307. https://doi.org/10.1139/e71-029

Orlanski, I. (1976). A simple boundary condition for unbounded hyperbolic flows. *Journal of Computational Physics*, *21*(3), 251–269. https://doi.org/10.1016/0021-9991(76)90023-1

Osher, S., Fedkiw, R., & Piechor, K. (2004). Level set methods and dynamic implicit surfaces. *Applied Mechanics Reviews*, *57*(3), B15. https://doi.org/10.1115/1.1760520

Osher, S., & Sethian, J. A. (1988). Fronts propagating with curvature-dependent speed: Algorithms based on Hamilton-Jacobi formulations. *Journal of Computational Physics*, *79*(1), 12–49. https://doi.org/10.1016/0021-9991(88)90002-2

Paterson, W. S. B. (1994). *Physics of glaciers*. Butterworth-Heinemann.

Peskin, C. S. (1972). *Flow patterns around heart valves: A digital computer method for solving the equations of motion*. Yeshiva University.

Peskin, C. S. (2002). The immersed boundary method. *Acta Numerica*, *11*, 479–517. https://doi.org/10.1017/S0962492902000077

Pettit, E. C., & Waddington, E. D. (2003). Ice flow at low deviatoric stress. *Journal of Glaciology*, *49*(166), 359–369. https://doi.org/10.3189/172756503781830584

Pettit, E. C., Waddington, E. D., Harrison, W. D., Thorsteinsson, T., Elsberg, D., Morack, J., & Zumberge, M. A. (2011). The crossover stress, anisotropy and the ice flow law at siple dome, west Antarctica. *Journal of Glaciology*, *57*(201), 39–52. https://doi.org/10.3189/002214311795306619

Qin, Z., Delaney, K., Riaz, A., & Balaras, E. (2015). Topology preserving advection of implicit interfaces on Cartesian grids. *Journal of Computational Physics*, *290*, 219–238. https://doi.org/10.1016/j.jcp.2015.02.029

Räss, L., Licul, A., Herman, F., Podladchikov, Y. Y., & Suckale, J. (2020). Modelling thermomechanical ice deformation using an implicit pseudo-transient method (FastICE v1. 0) based on graphical processing units (GPUs). *Geoscientific Model Development*, *13*(3), 955–976. https://doi.org/10.5194/gmd-13-955-2020

Räss, L., Utkin, I., Duretz, T., Omlin, S., & Podladchikov, Y. Y. (2022). Assessing the robustness and scalability of the accelerated pseudo-transient method. *Geoscientific Model Development*, *15*(14), 5757–5786. https://doi.org/10.5194/gmd-15-5757-2022

Rempel, A. (2008). A theory for ice-till interactions and sediment entrainment beneath glaciers. *Journal of Geophysical Research*, *113*(F1), F01013. https://doi.org/10.1029/2007jf000870

Rignot, E., & Mouginot, J. (2012). Ice flow in Greenland for the international polar year 2008–2009. *Geophysical Research Letters*, *39*(11), L11501. https://doi.org/10.1029/2012gl051634

Rignot, E., Mouginot, J., & Scheuchl, B. (2011). Ice flow of the Antarctic ice sheet. *Science*, *333*(6048), 1427–1430. https://doi.org/10.1126/science.1208336

Rignot, E., Vaughan, D. G., Schmeltz, M., Dupont, T., & MacAyeal, D. (2002). Acceleration of Pine island and Thwaites glaciers, west Antarctica. *Annals of Glaciology*, *34*, 189–194. https://doi.org/10.3189/172756402781817950

Robin, G. D. Q. (1955). Ice movement and temperature distribution in glaciers and ice sheets. *Journal of Glaciology*, *2*(18), 523–532. https://doi.org/10.3189/002214355793702028

Ryser, C., Lüthi, M. P., Andrews, L. C., Hoffman, M. J., Catania, G. A., Hawley, R. L., et al. (2014). Sustained high basal motion of the Greenland ice sheet revealed by borehole deformation. *Journal of Glaciology*, *60*(222), 647–660. https://doi.org/10.3189/2014jog13j196

Schmid, D. W., & Podladchikov, Y. Y. (2003). Analytical solutions for deformable elliptical inclusions in general shear. *Geophysical Journal International*, *155*(1), 269–288. https://doi.org/10.1046/j.1365-246x.2003.02042.x

Schoof, C., & Mantelli, E. (2021). The role of sliding in ice stream formation. *Proceedings of the Royal Society A*, *477*(2248), 20200870. https://doi.org/10.1098/rspa.2020.0870

Sergienko, O. (2012). The effects of transverse bed topography variations in ice-flow models. *Journal of Geophysical Research*, *117*, F03011. https://doi.org/10.1029/2011jf002203

Sethian, J. A. (1999). *Level set methods and fast marching methods: Evolving interfaces in computational geometry, fluid mechanics, computer vision, and materials science* (Vol. 3). Cambridge University Press.

Sethian, J. A., & Smereka, P. (2003). Level set methods for fluid interfaces. *Annual Review of Fluid Mechanics*, *35*(1), 341–372. https://doi.org/10.1146/annurev.fluid.35.101101.161105

Shapiro, N. M., & Ritzwoller, M. H. (2004). Inferring surface heat flux distributions guided by a global seismic model: Particular application to Antarctica. *Earth and Planetary Science Letters*, *223*(1–2), 213–224. https://doi.org/10.1016/j.epsl.2004.04.011

Suckale, J., Platt, J. D., Perol, T., & Rice, J. R. (2014). Deformation-induced melting in the margins of the west Antarctic ice streams. *Journal of Geophysical Research: Earth Surface*, *119*(5), 1004–1025. https://doi.org/10.1002/2013jf003008

Uhlmann, M. (2005). An immersed boundary method with direct forcing for the simulation of particulate flows. *Journal of Computational Physics*, *209*(2), 448–476. https://doi.org/10.1016/j.jcp.2005.03.017

Whillans, I., Bolzan, J., & Shabtaie, S. (1987). Velocity of ice streams B and C, Antarctica. *Journal of Geophysical Research*, *92*(B9), 8895–8902. https://doi.org/10.1029/jb092ib09p08895

Wright, A., Young, D., Roberts, J., Schroeder, D., Bamber, J., Dowdeswell, J., et al. (2012). Evidence of a hydrological connection between the ice divide and ice sheet margin in the aurora subglacial basin, east Antarctica. *Journal of Geophysical Research*, *117*(F1), F01033. https://doi.org/10.1029/2011jf002066

Yuen, D. A., & Schubert, G. (1979). The role of shear heating in the dynamics of large ice masses. *Journal of Glaciology*, *24*(90), 195–212. https://doi.org/10.3189/s002214300001474x

Zeitz, M., Levermann, A., & Winkelmann, R. (2020). Sensitivity of ice loss to uncertainty in flow law parameters in an idealized one-dimensional geometry. *The Cryosphere*, *14*(10), 3537–3550. https://doi.org/10.5194/tc-14-3537-2020